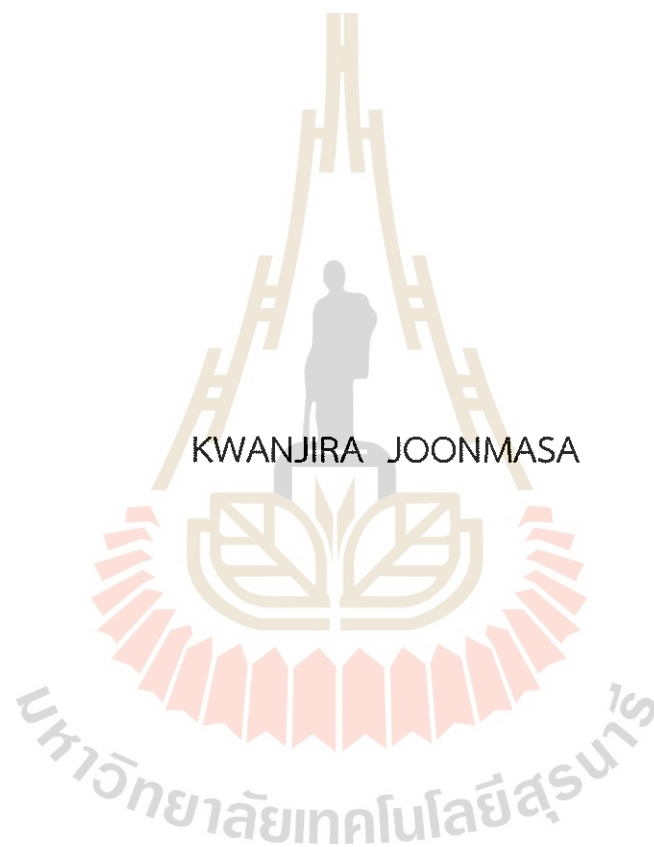# DESIGN AND ANALYSIS OF HOLLOW CORE ANTIRESONANT FIBER FOR ETHYLENE DETECTION

KWANJIRA JOONMASA

A Thesis Submitted in Partial Fulfillment of the Requirements for the
Degree of Master of Science in Applied Physics
Suranaree University of Technology
Academic Year 2022

การออกแบบและวิเคราะห์เส้นใยแก้วนำแสงกลวงที่มีโครงสร้างแบบแอนไทเรโซแนนซ์สำหรับการตรวจจับก๊าซเอทิลีน

นางสาวขวัญจิรา จุลมาษา

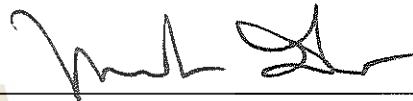# DESIGN AND ANALYSIS OF HOLLOW CORE ANTIRESONANT FIBER FOR ETHYLENE DETECTION

Suranaree University of Technology has approved this thesis submitted in partial fulfillment of the requirement for a Master's Degree.
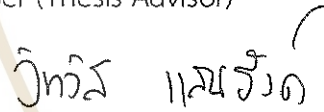
Thesis Examining Committee

_____

(Dr. Wiwat Nuansing)

Chairperson

_____

(Assoc. Prof. Dr. Panomsak Meemon)

Member (Thesis Advisor)

_____
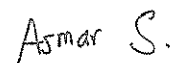
(Asst. Prof. Dr. Wittawat Saenrang)

Member

_____

(Prof. Dr. Joewono Widjaja)

Member

_____

(Dr. Asmar Sathukarn)

Member

_____
(Assoc. Prof. Dr. Yupaporn Raksakulpiwat)
Vice Rector for Academic Affairs
and Quality Assurance

_____
(Prof. Dr. Santi Maensiri)
Dean of Institute of Science

ขวัญจิรา จุลมาษา : การออกแบบและวิเคราะห์เส้นใยแก้วนำแสงกลวงที่มีโครงสร้างแบบ
แอนไทเรโซแนนซ์สำหรับการตรวจจับก๊าซเอทิลีน (DESIGN AND ANALYSIS OF HOLLOW
CORE ANTIRESONANT FIBER FOR ETHYLENE DETECTION) อาจารย์ที่ปรึกษา :
รองศาสตราจารย์ ดร.พนมศักดิ์ มีมนต์, 84 หน้า

คำสำคัญ: เซ็นเซอร์ใยแก้วนำแสง, เส้นใยแก้วนำแสงกลวงที่มีโครงสร้างแบบแอนไทเรโซแนนซ์,
    การตรวจจับก๊าซเอทิลีน

ในช่วงทศวรรตที่ผ่านมาเส้นใยแก้วนำแสงสำหรับนำคลื่นในย่านอินฟาเรดช่วงกลางได้รับ
ความสนใจเป็นอย่างมากเนื่องจากความสามารถในการนำไปประยุกต์ใช้ได้ในงานที่หลากหลาย
โดยเฉพาะอย่างยิ่งในการตรวจจับก๊าซเอทิลีนซึ่งเป็นหนึ่งในก๊าซสำคัญที่ถูกปล่อยออกมาจากผลไม้
และดอกไม้ในระหว่างกระบวนการสุก ดังนั้น การควบคุมและการตรวจจับก๊าซชนิดนี้จึงมีความสำคัญ
ต่ออุตสาหกรรมการจัดเก็บและส่งออกผลไม้และดอกไม้ การตรวจจับก๊าซโดยใช้เส้นใยแก้วนำแสง
แบบแกนกลวงเป็นหนึ่งในเทคนิคที่น่าสนใจ เนื่องจากโครงสร้างภายในของเส้นใยแก้วนำแสงชนิดนี้ที่
เป็นท่อกลวงระดับไมโครเหมาะสำหรับการไหลผ่านของก๊าซในปริมาณที่ไม่มากได้ ด้วยเหตุนี้ งานวิจัย
นี้จึงมุ่งเน้นไปที่การออกแบบและวิเคราะห์เส้นใยแก้วนำแสงแบบแกนกลวงที่มีโครงสร้างแบบแอน
ไทเรโซแนนซ์สำหรับการตรวจจับก๊าซเอทิลีน ซึ่งใยแก้วนำแสงที่นำเสนอในงานวิจัยนี้ประกอบไปด้วย
ส่วนหุ้มหกท่อกลวงที่ล้อมแกนกลางกลวงเอาไว้ โดยในงานวิจัยนี้ได้ทำการจำลองโหมดของแสงในเส้น
ใยแก้วนำแสงโดยทำการปรับโครงสร้างให้เหมาะสมเพื่อให้ได้การสูญเสียของสัญญาณแสงที่เดินทางใน
เส้นใยแก้วนำแสงที่ต่ำโดยในงานวิจัยเส้นใยแก้วนำแสงถูกออกแบบมาเพื่อให้นำแสงที่ความยาวคลื่น
3.2 ไมโครเมตร ซึ่งเป็นความยาวคลื่นที่สอดคล้องกับแถบการดูดกลืนแสงของก๊าซเอทิลีน โดยผลการ
จำลองแสดงให้เห็นว่าเส้นใยแก้วนำแสงที่ถูกออกแบบในงานวิจัยนี้มีการสูญเสียสัญญาณประมาณ 2
เดซิเบลต่อเมตร เมื่อเส้นผ่านศูนย์กลางแกนเส้นใยแก้วนำแสงคือ 128 ไมโครเมตร โดยความหนาและ
เส้นผ่านศูนย์กลางของท่อกลวงภายในเท่ากับ 2 ไมโครเมตร และ 92 ไมโครเมตร ตามลำดับ การ
จำลองการใช้เส้นใยแก้วนำแสงเพื่อการตรวจวัดความเข้มข้นของก๊าซเอทิลีนในงานวิจัยนี้พบว่าเมื่อ
ความเข้มข้นของก๊าซเอทิลีนในแกนกลางเปลี่ยนไปเส้นใยแก้วนำแสงที่ออกแบบมานี้จะมีความไวของ
ดัชนีการหักเหของแสงอยู่ที่ 5.68 ไมโครเมตรต่อหน่วยของดัชนีหักเห

สาขาวิชาฟิสิกส์   ลายมือชื่อนักศึกษา_____
ปีการศึกษา 2565   ลายมือชื่ออาจารย์ที่ปรึกษา_____

KWANJIRA JOONMASA : DESIGN AND ANALYSIS OF HOLLOW CORE ANTIRESONANT FIBER FOR EHYLENE DETECTION.

THESIS ADVISOR : ASSOC. PROF. PANOMSAK MEEMON, Ph.D. 84 PP.

Keyword: Optical fiber sensor, Hollow core antiresonant fiber, Ethylene detection

An optical fiber for mid-infrared (mid-IR) guidance has long attracted great interest due to its wide range of applications, especially in gas sensing. Ethylene gas (C_2H_4) is one of the important gases that is released from the fruit and flower, owing to their ripening process. Thus, the control and detection of ethylene gas are of interest for the storage and exportation of fruits and flowers. Gas detection using hollow-core optical fiber (HCF) is a promising technique due to its intrinsic micro-channel structure that allows the gas to flow through the HCF for detection purposes. Here, a hollow-core anti-resonant fiber (HC-ARF) is designed and optimized for mid-IR guidance for ethylene detection. The HC-ARF includes 6 cladding tubes that are optimized to achieve a low confinement loss at a wavelength of 3.2 μm (ethylene absorption wavelength). The simulation result shows that a confinement loss of 2 dB/m at the wavelength of 3.2 μm can be achieved when the fiber core diameter is 128 μm and the thickness and the diameter of the cladding tubes are 2 μm and 92 μm, respectively. The optimized fiber from this work provided the refractive index sensitivity of 5.68 μm/RIU when the ethylene with different concentration is filled in the hollow core of the optical fiber.

School of Physics

Academic Year 2022

Student's Signature _____

Advisor's Signature _____

ACKNOWLEDGMENTS

CONTENTS

CONTENTS (Continued)

LIST OF TABLES

LIST OF FIGURES

LIST OF FIGURES (Continued)

LIST OF FIGURES (Continued)

LIST OF ABBREVIATIONS

IR	Infrared
HCF	Hollow-core optical fiber
HC-ARF	hollow-core anti-resonant fiber
RIU	Refractive index unit
MOFs	Microstructure optical fibers
SC-PCF	Solid-core photonics crystal fiber
HC-PCF	Hollow-core photonics crystal fiber
RI	Refractive index
GC	Gas chromatography
FEM	Finite elements methid
LP	linearly polarized
SMF	Single mode fiber
SEM	Scanning electronic microscopy
MPOF	Microstructured polymer optical fibers
FM	Fundamental mode
HC-NANF	Hollow-core nested anti-resonant node free fiber
NDIR	Non-dispersive infrared
PAS	Photo-acoustic spectroscopy
PML	Perfect match layer
TIR	Total internal reflection
NA	Numerical aperture
EM	Electromagnetic
TEM	Transverse electromagnetic
TE	Transverse electric
TM	Transverse magnetic

LIST OF ABBREVIATIONS (Continued)

UV	Ultraviolet)
PCF	Photonics crystal fiber
PBGF	Photonic bandgap fibers
SPR	surface plasmon resonance
THz	Terahertz
FBG	Fiber Bragg grating
FIB	Focused ion beam
MMF	Multimode fiber
OFS	Optical fiber sensors
RIMLs	Refractive index matching liquids
ARROW	anti-resonant reflecting optical waveguide
LPG	Long period grating
DAS	Direct absorption spectroscopy
WMS	Wavelength modulation spectroscopy
PTS	Photothermal spectroscopy
FTS	Fourier transform spectroscopy
CLDS	Chirped laser dispersion spectroscopy
SRCS	Spontaneous Raman scattering spectroscopy
RCS	Raman scattering spectroscopy
SRGS	Stimulated Raman gain spectroscopy
PET	Polyethylene terephthalate
PMMA	Polymethyl methacrylate

CHAPTER I

INTRODUCTION

An optical fiber is a widely used device in data transfer due to its low power loss and good robustness. Therefore, the optical fiber technology has become an important part of the innovation in telecommunication. In 2021, hundreds of millions kilometers of the single mode silica optical fiber spanned over our globe to support an increasing of data traffic each year (Cisco, 2017). However, long-haul data transmission is not the only application where optical fibers are of great use. There is also a vast variety of short-range optical fiber applications which are of interest. Thus, many designs of optical fibers have been proposed for sensing applications. Various types of optical fiber sensors have been developed by modifying the structure of the fiber core and the cladding to increase the interaction between the guided light and the surrounding environment.

Conventional step-index optical fiber consists of a core with a higher refractive index, surrounded by a cladding with a lower refractive index. Light in the conventional step-index optical fiber is guided through total internal refraction (TIR) at the interface between core and cladding. Although the conventional step-index fiber has been successfully used in many applications, solid core of theses fibers is their limitations owing to the fundamental limits imposed by the interaction between the propagating optical waves and the core's materials. Thus, the propagating waves inside the fiber will be slow down and their intensity will be dissipated due to scattering and material absorption loss. Solid core fiber also has an issue when guiding the light with high optical power. When the power of guided light is high, the oscillatory response of bound electrons of guided material molecules is no longer proportional to the driving optical field, leading to the appearance of a nonlinear effect. Moreover, the generated heat due to the high power of the guided light can cause damage to the fiber core, resulting in a high loss (Ismail, 2009).

Unlike conventional optical fibers, which are a solid combination of glasses with different refractive indices, a novel type of optical fiber, known as a microstructured optical fiber (MOF) is made of one material with the introduction of microscopic air holes that run along the entire length of the optical fiber. Microstructure optical fiber is the fiber with a microstructure in which air-holes are introduced in the core or cladding region and extend in the axial direction of the fiber. The MOFs come in a variety of different core shapes, core and cladding sizes, and distributions of airholes. Due to an intrinsic air-holes inside the MOF, it is also interested in sensing applications. The MOF can be divided into two types based on the core structure, i.e., solid-core and hollow-core MOF. To overcome the limitations of solid core fiber as presented before, hollow-core fibers (HCF) are of great interest to researchers. Light in the HCF will be guided in an air-filled core that is surrounded by a microstructured cladding designed to confine light to the core of the fiber. Light guidance in air afforded by HCF opens new opportunities in vast variety of applications. Air-core of HCF is the ideal medium in which light can propagate free of interactions with a solid material that decrease the power of light and increasing the guided loss, thereby limiting the data-carrying capacity. Furthermore, they offer an ideal platform for delivering intense radiation without non-linear distortions or damage to the fibers. HCFs also allow for controlled interactions between light and gases inside the fiber core, which can be an ideal guiding medium for gas sensing applications.

Among many gas sensing applications, Ethylene gas (C_2H_4) is one type of plant hormone that can release in different development stages in plants, fruits, and flowers. The senescence of flowers and leaves relate to the releasing of ethylene gas. Moreover, the binding of ethylene gas with receptor in plants cause the increasing of speed in ripening process of fruits. The high concentration of ethylene releasing can signify increase some inappropriate features in fruits like flimsy and squashy leading to the difficulty in storage and transportation fruits. Therefore, the ethylene gas monitoring during the storage and transportation of fruits and flowers is of interest for researchers to develop the gas sensing device for the fruit and flower transportation market.

In the past decade, research in microstructured optical fibers (MOF) has been increased by the wide variety of proposed geometries and their potential applications. Due to the intrinsic presence of air holes, index modulation in MOFs can be easily achieved. Therefore, these optical fibers have been investigated for many applications, especially for sensing. Among all optical sensing schemes, the use of mid-infrared (MIR) is gaining strong attention, especially for biological and chemical applications. This is

attributed to the high inherent molecular selectivity and strong signal of optical sensing schemes.

This research project focused on the design and the optimization of the structure of hollow-core microstructure optical fiber, aiming for ethylene sensing applications at MIR region. The simulation of the hollow-core MOF with anti-resonant structure was performed to analyze the optical properties and optimize the fiber structure to achieve the lowest guiding loss at a specific wavelength of 3.2 μm to be matched with absorption wavelength of ethylene gas.

More details about the light-guiding mechanism of MOF, research procedure, and simulation result will be described in chapters 2, 3, and 4 respectively.

1.1 Research objectives

This thesis aims to design and optimize the structure of the hollow-core optical fiber with an anti-resonant structure by using COMSOL Multiphysics software. The purpose for the structure optimization is to achieve low confinement loss at 3.2 μm in which related to the absorption spectrum of ethylene gas.

1.2 Research hypothesis

- From the literature review, hollow-core antiresonant fiber (HC-ARF) with nested structure revealed the lowest loss for the c-band regime. So, we expect this structure will get a lower loss than non-nested structure with our operating wavelength (3.2 μm) and Polyethylene terephthalate (PET) material.
- The finite elements method (FEM), it is the numerical method that used in this work is divided the domain structure into subdomains, so we believe that smaller subdomain sizes will provide more accurate simulation results.
- The simulation model needs to have the artificial layer surround our fiber structure to mimic the real environment. the artificial absorbing layer known as the perfect match layer (PML) is very important for calculating the leakage loss of fiber. So, we expect that we can optimize the distance of the PML layer to get low-loss fiber.
- For ethylene sensing, the optimized structure of hollow-core anti-resonant optical fiber can detect the shift of resonance wavelength due to the refractive index changing directly with the concentration of ethylene gas.

1.3 Thesis outline

The purpose of this introduction is to highlight the interesting structure of MOFs over conventional optical fibers, particularly HC-MOFs, and to emphasize that this type of fiber is suitable for liquid or gas sensing applications. The remaining sections of this thesis are arranged as follows:

Chapter II presents an overview of each type of optical fiber: conventional optical fiber, solid-core photonic crystal fiber (SC-PCF), hollow-core photonic crystal fiber (HC-PCF), and hollow-core antiresonant fiber (HC-ARF), consisting of their structure, light guiding mechanism, fabrication, and applications.

Chapter III presents the mode field distribution that is guided in the fiber core and the method in COMSOL multiphysics software to get the confinement loss of a fiber structure consisting of geometry modeling, finite elements method (FEM), and perfect match layer (PML).

Chapter IV presents the research results and discussion. The optimized structure after changing parameters of the fiber structure, such as core diameter (D_c), and cladding tube thickness (t). The next results are the effect of changing cladding materials and the effect of core refractive index.

Chapter V presents an overall summary of this research and an outlook for future work.

Appendix presents the details of conventional optical fiber, the refractive index of fiber material, and the calculation of the refractive index of ethylene gas when concentration changes.

CHAPTER II

LITERATURE REVIEWS

2.1 Ethylene detection

Ethylene gas (C_2H_4) is one type of plants hormone that releases while plants ripening. The concentration of ethylene releasing can signify the step of ripening and changing the texture, color, and soften in some types of plant. Because of its property, ethylene is very important gas to be monitored for fruits and flowers transportation. Therefore, several methods are innovated for ethylene detection, including gas chromatography (GC), electrochemical sensing, and optical sensing.

2.1.1 Gas chromatography (GC)

Gas chromatography (GC) is a chemical analysis device used to separate the individual gas component in a sample as illustrated in figure 1. The GC system has carrier gas always moving in the system. In the analysis, the sample is taken into the GC via the injection port located within the temperature controller chamber. There is a closed system to prevent gas leakage. Under the high temperature of the injection port, the sample is vaporized and moved along the column with the carrier gas. Inside the column, which has a fixed phase coated on solid supports or coating on the pipe, the organic matter in the sample exerts a force on a fixed phase with different organic properties. Each type of organic substance has a different force, resulting non equally bind in a fixed phase for each organic substance. Therefore, the organic matter is separated within this column, and finally, the organic matter travels out of the column into the signal probe at different times. The measured signal will be converted to an electrical signal electronically and sent to the processing and saving section. (Cristescu, Mandon et al., 2013)
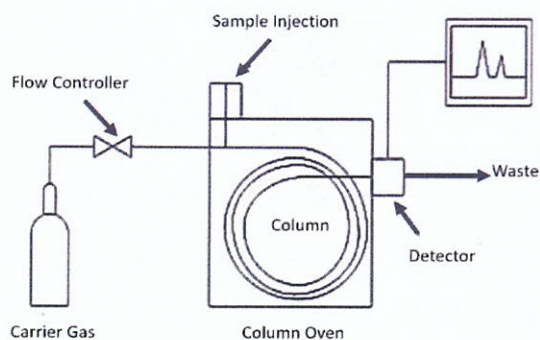
Figure 1 Diagram of gas chromatographic method. There are three main GC system components: the sample injection unit, which heats the liquid sample and vaporizes it; the column, which is used to separate each compound; and the detector, which detects the compounds and outputs their concentrations as electrical signals. (Kathirvelan and Vijayaraghavan, 2020)

2.1.2 Electrochemical sensing

The gas detection in the electrochemical sensor is based on the changing of the gas concentration into a detectable physical signal such as electrical current, resistance, etc. In electrochemical sensor system, the active sensing material on the sensor will be designed to have a chemical interaction with the interesting gas of the active sensing device will be connected to an electrical circuit in which a change in an electrical parameter will be generated due to the chemical change in the active sensing material.

Type of electrochemical sensors can be categorized by the physical change measured, measure current (A) is refer to "Amperometric sensors", the measurement of resistance (Ω) will be referred to "Chemo resistive sensors", and the measurement of a change in capacitance of the sensors will be called "Capacitive sensor". Figure 2 shows the example of Amperometric sensors. In the system, Ethylene gas spread through the barrier into the sensor, which consists of the detection electrode (Anode, A), counter electrode (Cathode, C), and reference electrode (R) covered with a thin layer of electrolyte solution (E). Ethylene will be catalytically oxidized when the electrical potential is applied to the anode. Therefore, the current changes are proportional to the ethylene concentration. (Cristescu, Mandon et al., 2013)
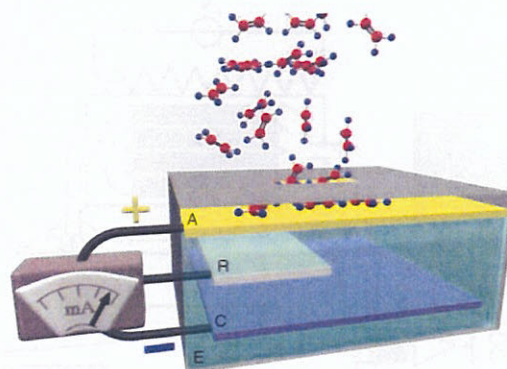
Figure 2 Example of Amperometric sensos. Ethylene diffuses through a barrier into the sensor, which consists of a sensing electrode (anode, A), a counter electrode (cathode, C) and a reference electrode (R) covered by a thin layer of an electrolytic solution (E). If an electrical potential is applied to the anode (most recently made of gold particles) ethylene is catalytically oxidized, resulting in a current change proportional to the ethylene concentration. (Cristescu, Mandon et al., 2013)

2.1.3 Optical sensing

When light interacts with the gas molecules it can be emitted, scattered, and absorbed. Each gas molecule absorbs light with a specific wavelength. For Ethylene gas, their absorption range is 2-10 µm or mid-Infrared (Cristescu, Mandon et al., 2013). Due to the specific absorption wavelength of Ethylene, several optical sensing methods can be innovated for the Ethylene detection.

Non-dispersive infrared (NDIR) gas sensor

A nondispersive infrared sensor (NDIR) is a simple spectroscopic sensor. It is non-dispersive system because there is no dispersive element, such as a prism or grating, in the system. The NDIR is used to separate the broadband light into a narrow spectrum by using a broadband light source (lamp) and an optical filter to select a narrow band that overlaps with the absorption region of the gas of interest. In 2012, Sklorz et al. proposed the ethylene detection using NDIR gas sensor merged with pre-concentrator using the experimental setup shown in figure 3. In their experiment, infrared (IR) source with the wavelength of 10.5 µm was coupled with thermopile detectors through IR filters and focal lenses enclosed in a gas test cell. To overcome sensitivity limitations, the system was additionally combined with an ethylene pre-concentrator to increase the system sensitivity down to the ppbv (parts per billion by volume) region indirectly by using adsorption effects on graphitized carbon. This system measures ethylene down to 10 ppmv (parts per million by volume). (Kathirvelan and Vijayaraghavan, 2020)
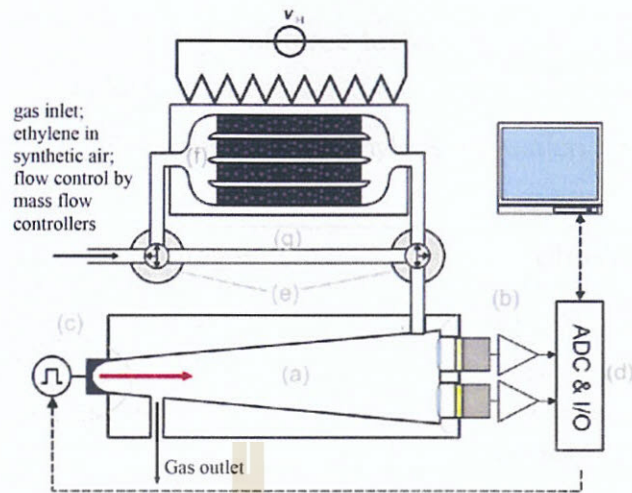
Figure 3 NDIR gas sensor merged with preconcentrator using the experimental set-up. (a) NDIR measurement chamber, (b) thermopile detectors and amplifiers, (c) IR source, (d) Data acquisition module, (e) Controlled valves, (f) Pre-concentrator device, (g) Bypass. (Sklorz, Janssen et al., 2012)

In Photo-acoustic spectroscopy (PAS) method, a broadband light source will be shone through a filter wheel (A) or using a monochromatic laser (B) without the filter as presented in figure 4. Light direct into an absorption cell, where it is absorbed by the ethylene molecules, will be converted into heat. By switching the light on and off with a mechanical chopper, the temperature changes periodically, giving rise to a periodic pressure change, resulting in acoustic energy detected by a miniature microphone. The intensity of the sound is proportional to the concentration of absorbing gas molecules present in the cell. (Cristescu, Mandon et al., 2013)
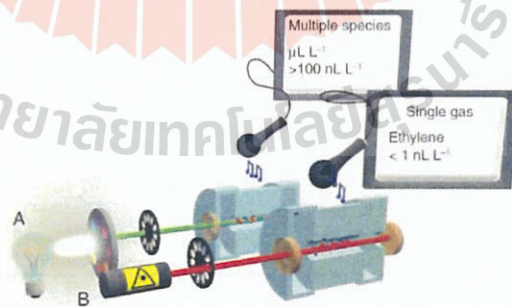
Figure 4 Simple diagram for photoacoustic spectroscopy (PAS) (Cristescu, Mandon et al., 2013)

Advantages and disadvantages of three techniques that mentioned above are summarized in the table below.

Table 1 Advantages and disadvantages of ethylene detection method. (Cristescu, Mandon et al., 2013)

Methods	Advantages	Disadvantages
Gas Chromatography (GC)	• Small sample requirements • High selectivity • good at separating complex mixtures and compounds	• Limited sensitivity • Requires a pre-concentration step for better sensitivity and optimized plant conditions. • High costs for the highest performing systems
Electrochemical Sensing	• Good repeatability and accuracy • Low power consumption • Lightweight (2.5–10 kg) • Low cost	• Sensitive to interfering gases. • Sensitivity to temperature and humidity changes • Reduced lifetime when continuously exposed to higher ethylene concentrations.
Optical Sensing	• Highest sensitivity (below nL^{-1}) • Fastest response time (seconds) • Good selectivity • Real-time monitoring	• Expensive • Single gas detection

Besides all methods described above, the new method that provide a smaller, lighter weight, and uses a small amount of gas for detection is the optical fiber sensors.

Figure 5 shows an example of an optical fiber sensor setup. It is a laser-based dual gas sensor employing a silica-based HC-ARF working in the Near- and Mid-Infrared spectral regions. Using the simple and well-known Wavelength Modulation Spectroscopy (WMS) technique, a 1-m-long fiber with an 84-µm-diameter air core was used as a low-volume absorption cell in a sensor configuration. The fiber was filled with a mixture of methane (CH_4) and carbon dioxide (CO_2), and simultaneous detection of both gases was demonstrated by focusing on their respective transitions at 3.334 µm and 1.574 µm. The proposed sensor achieved a detection limit of 24 ppm for CH_4 and 144 ppm for CO_2 owing to the good guiding properties of the fiber and reduced background noise. (Jaworski, Kozioł et al., 2020)
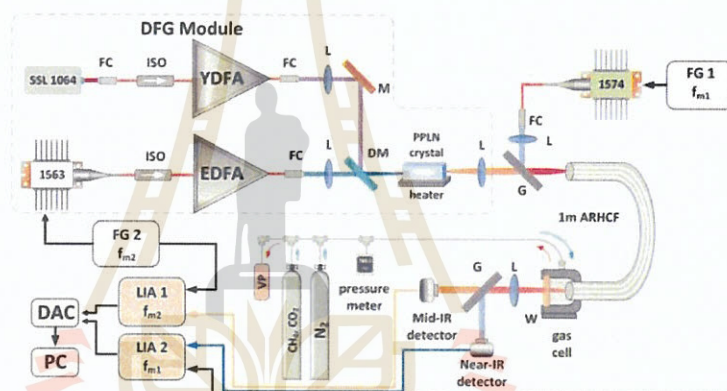
Figure 5 Schematic of the experiment set up. (Jaworski, Kozioł et al., 2020)

As mentioned in chapter 1, this research will be focused on the optical fiber design for the optical fiber sensor technology. Therefore, type of optical fiber structure that used in this work are presented.

2.2 Microstructure optical fibers (MOFs)

Microstructure optical fibers (MOFs) or photonic crystal fibers (PCFs) are typically all silica optical fibers in which air-holes are introduced in the core or cladding regions which extend along the length of the fiber. The MOFs come in a variety of different shapes, sizes, and distributions of air-holes.

Figure 6 shows the physical structure and parameters of conventional optical fiber (a) and photonic crystal fiber (b and c). The physical parameters in which corresponding with the light guiding mechanism in the optical fiber are varied with the fiber structure. In the conventional optical fiber, the confinement of light in the fiber is only depends

on the core diameter (ρ). For, the photonic crystal fiber, the confinement of light depends on many parameters, including the core diameter (ρ), the diameter of the air hole in the cladding region (d), and the arrangement of the air-holes in the cladding, which is the distance between the center of two consecutive air holes or the pitch (Λ). These parameters make the microstructure optical fiber have various structures and flexibility in design to suit each application. Due to the flexibility in design of the PCFs, air-guided optical fiber or hollow-core fiber has been introduced through the design of PCFs. Hence, the PCFs can differentiated into 2 types based on the guiding medium including solid-core PCFs and hollow-core PCFs.
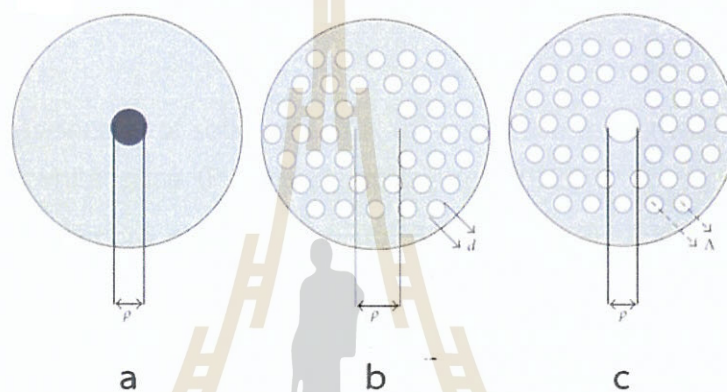
Figure 6 The cross-section of (a) single-mode fiber (SMF), (b) solid-core photonic crystal fiber (SC-PCF), and (c) hollow-core photonic crystal fiber (HC-PCF). Colors: blue: silica, grey: doped silica, white: air. (Pinto and Lopez-Amo, 2012)

2.2.1 Solid-core photonics crystal fiber (SC-PCF)

The photonic crystal fiber (PCF) traditionally has a periodic structure of air holes in the cladding region. For solid-core photonic crystal fiber (SC-PCF), the light guidance mechanism is still based on the total internal reflection (TIR) principle. The refractive index of the solid core is surely higher than the effective refractive index of the cladding, as shown in figure 7(b), and this guidance mechanism is called modified total internal reflection (MTIR).
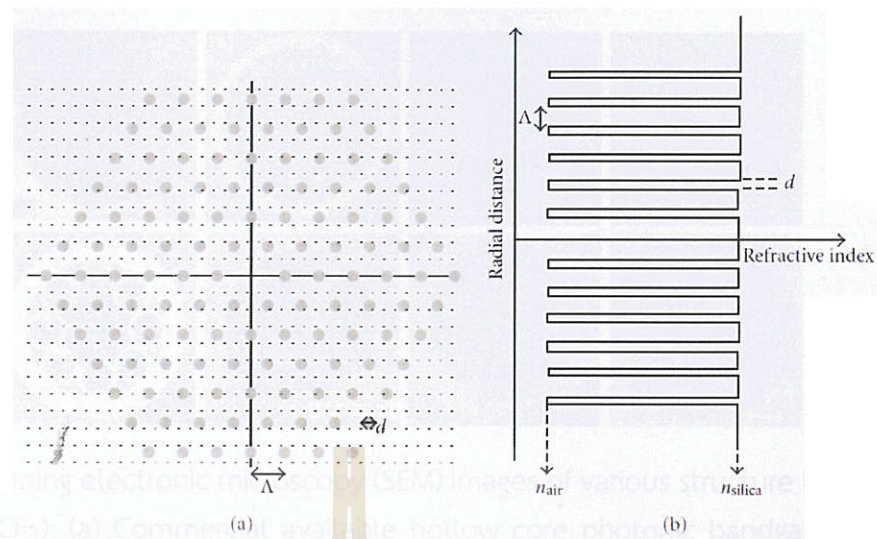
Figure 7 (a) cross-section of solid-core PCF, (b) respective refractive index profile, and colors: grey: air, white: silica. (Pinto and Lopez-Amo, 2012))

2.2.2 Hollow-core photonics crystal fiber (HC-PCF)

For the Hollow-core photonic crystal fiber (HC-PCF), the fiber core has a refractive index lower than the effective refractive index of the cladding, as shown in figure 8(b). Therefore, the total internal refraction principle (TIR) cannot be applied for the light guiding this fiber. The guidance mechanism depends on the individual structure of the fiber, such as photonics bandgap guiding mechanism for the photonic bandgap fiber or antiresonance guiding mechanism for the anti-resonant fiber. (Arismar Cerqueira, 2010)
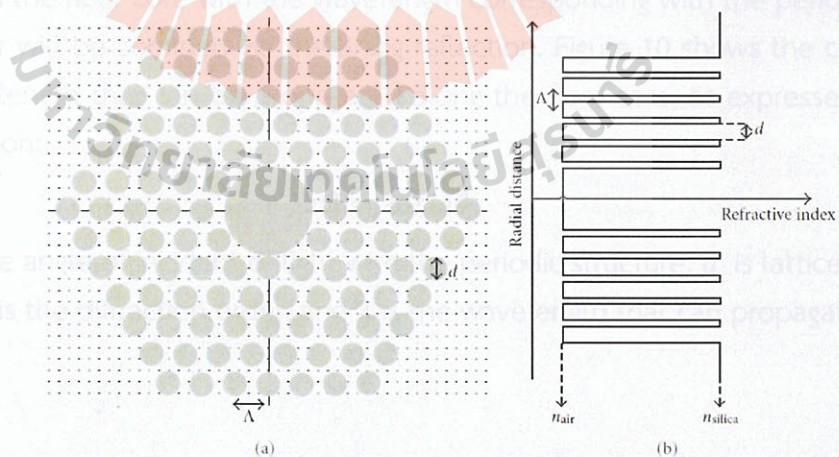
Figure 8 (a) cross-section of hollow-core PCF, (b) respective refractive index profile, and colors: grey: air, white: silica. (Pinto and Lopez-Amo, 2012)
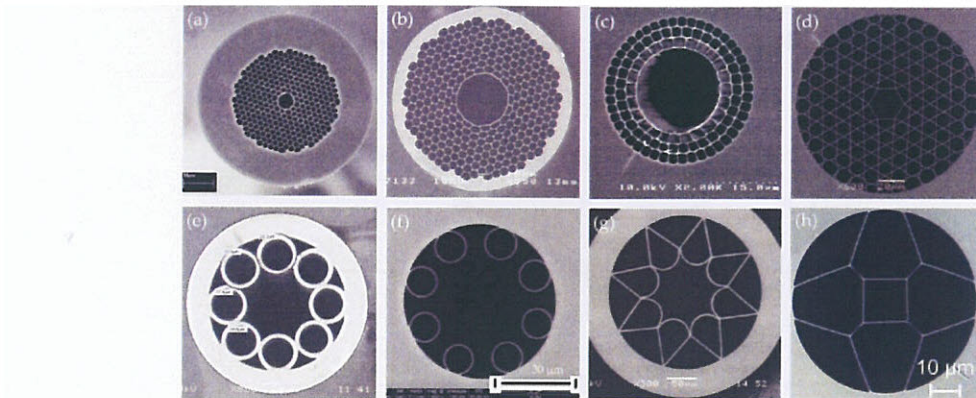
Figure 9 Scanning electronic microscopy (SEM) images of various structure hollow-core fibers (HC-PCFs): (a) Commercial available hollow core photonic bandgap fiber (HC-PBGF): HC-1550-02 from NKT Photonics, (b) HC-PCF designed for the guiding in the MIR region, (c) Hollow core Bragg fiber, (d) Kagome lattice HC-PCF, (e) hollow core antiresonant fibers (HC-ARF), (f) nodeless HC-ARF, (g) hollow fiber with negative curvature of the core wall, (h) double anti-resonant hollow square core fiber. (Yu, Chen et al., 2020)

Figure 9(a)-(c) show the photonic bandgap fibers which are one type of the hollow-core photonic crystal fiber. The photonics bandgap fiber (PBGF) are the optical fibers, where the light can be guided by the photonic bandgap effect. The light guiding in the PBGF can be confined by the Bragg scattering principle. In the PBGF, the cladding region will be formed with the periodic layers as presented in figure 9. The light propagates in the fiber core with the wavelength corresponding with the period of the periodic layer will be confined via the Bragg reflection. Figure 10 shows the condition for the wavelength that can be propagated along the fiber core, as expressed in the below equation:

$$n\lambda = 2d\sin\theta . \tag{1}$$

where θ is the angle of incident of light with the periodic structure, d is lattice spacing (figure 15), n is the diffraction order, and λ is the wavelength that can propagate in the fiber core.
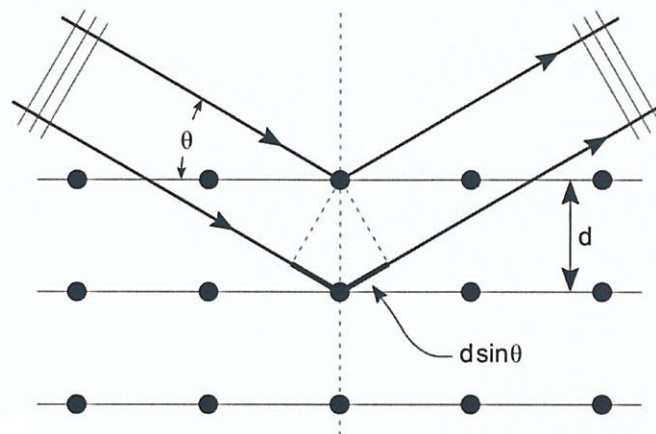
Figure 10 Bragg scattering principle. (Wikipedia, 2023b)

Figure 10 shows the Bragg scattering condition, two light rays with the same wavelength and phase approach a crystalline solid and are scattered off two different atoms within its structure. The beam with longer travelling distance will travel an extra length of $2dsin\theta$. So, to conserve a constructive interference, the optical path different ($2dsin\theta$) must be equal to an integer number multiply by the wavelength of the radiation. Therefore, this principle can be used to explain the propagation of light in the PBGF that only the constructive interference light can propagate into the core of the fiber.

Figure 9(d)-(f) shows another type of hollow-core fiber in which the light propagate in this type of fiber is confine by antiresonance effect, so call "Anti-resonant fiber (ARF)". For the ARF, the thin layer surrounds the fiber hollow-core will perform the two-parallel layers in which behave as a Fabry-Perot etalon for the Fabry-Perot interferometer as shown in figure 11. The hollow-core surround (thin membrane) provides high reflection of the antiresonance light to confine and guide light in the hollow-core. The transmission and the reflection coefficients of the interference of light in the thin membrane depend on the wavelength of the light in the fiber, the thickness, and the refractive index of the of thin membrane. The wavelength that will be transmitted through the thin membrane into the cladding cavity are the resonance wavelengths. While, the non-resonance will be reflected and propagated in the fiber core, so call antiresonance wavelength. (Putten, 2019)
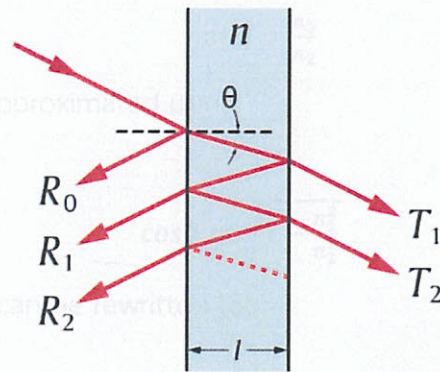
Figure 11 A Fabry–Pérot etalon. Light enters the etalon and undergoes multiple internal reflections. (Wikipedia, 2023c)

To find the resonance condition, the transmission (T) and reflection (R) coefficient will be considered. The relationship between the transmission and reflection in the thin membrane (figure 11) with the thickness (t) and refractive index (n) of the thin membrane can be express in equation (4). Another essential parameter is the refractive index of the core and the surrounding medium. Such a thin membrane behaves as a Fabry-Perot etalon whose transmission coefficient (T) depends on the reflectivity of each interface, the transmission coefficient for a thin membrane is defined as (Putten, 2019)

$$T = \frac{(1-R)^2}{(1-R)^2 - 4R\sin^2(\delta)}, \tag{2}$$

where R is reflection coefficient at a single air-membrane interface. The phase difference (δ) can be given as (Putten, 2019)

$$\delta = \frac{2\pi n_2 l\cos(\theta)}{\lambda}, \tag{3}$$

A maximum in transmission occurs when the phase difference satisfies the following condition (Putten, 2019):

$$\delta = \frac{2\pi n_2 l\cos(\theta)}{\lambda} = m\pi, \text{ for } m = 1, 2, 3, .. \tag{4}$$

At incidence angle between medium and a thin membrane surface approaches to 90 degrees respective to the normal line. The angle of refraction can be determined by using Snell's law, and one obtains:

$$sin\theta = \frac{n_1}{n_2} \quad . \tag{5}$$

Therefore, $cos\theta$ can be approximated using:

$$cos\theta = \sqrt{1 - \frac{n_1^2}{n_2^2}} \quad . \tag{6}$$

So, the phase difference can be rewritten to:

$$\delta = \frac{2\pi l}{\lambda} \sqrt{n_2^2 - n_1^2} \quad . \tag{7}$$

Using Equation (7), the resonance wavelengths can be expressed as:

$$\lambda_m = \frac{2l}{m} \sqrt{n_2^2 - n_1^2} \quad . \tag{8}$$

Therefore, the resonance wavelength that will be transmitted through the thin membrane or Fabry-Perot etalon can be calculated by using equation (8).

Figure 12 shows the loss-dependence of hollow-core antiresonant triangular-core fibers with the thickness of core surround (t_1) = 2.19 μm, and λ = 2.94 μm. Considering graph at wavelengths of 1.125, 1.5, and 2.25 μm showing a high loss. These high loss wavelengths indicate the resonance wavelength corresponding with equation (8). At these wavelengths, the light will resonance with the thickness of the thin membrane surrounds the fiber core and transmit to the cladding region. Thus, the window the anti-resonant wavelength will be reflected to the fiber core which can be propagated in the fiber core showing the low loss at these wavelengths.
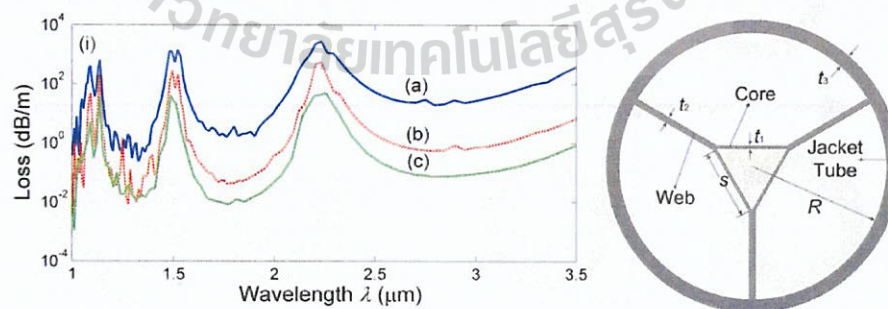
Figure 12 Loss-dependence of hollow-core antiresonant triangular-core fibers on the jacket tube thickness t_3, with t_1 = 2.19 μm and λ= 2.94 μm. Straight blue, dashed dotted red, and dashed green lines represent the fibers (a), (b), and (c) with side lengths s = 40, 70, and 100 μm. (Chen, Saleh et al., 2016)

As we mentioned in the research objectives, the structure of optical fiber in this work is the hollow-core antiresonant fiber (HC-ARF) due to its lower loss comparing with another type of hollow core fiber. Moreover, this simple structure is easy to fabricate and has a hollow core for flowing gas. So, the literature review of HC-ARF design will be presented and the summarization of the property of this structure are presented in the subsection below.

2.3.2.1 Hollow-core antiresonant fiber (HC-ARF) design. Since 2011, many structures of hollow-core antiresonant fiber (HC-ARF) have been reported. In 2002, 7-cell PBGF (figure 13(a)) with loss of 13 dB/km was presented, while, in 2005, the fiber loss improved to 1.2 dB/km for 13-cell PBGF (figure 13(b)). A new type of HCF was proposed in 2002, so call Kagome HCF (figure 13(e)) with loss of <2000 dB/km. It is a highly delicate structure of thin triangular-lattice struts with no cladding nodes. In 2010, the negative curvature Kagome, called hypocycloid fibers (figure 13(f)) was invated, and improved loss to <250 dB/km. In 2011, the simplest design was developed, called tubular ARF (figure 13(c)), with loss <1000 dB/km. In 2017, the loss of ARF was reduced to 7.2 dB/km. In 2020, the structure called nested nodeless ARF (figure 13(h)) showing that the fiber loss can be decreased to 0.28 dB/km by adding the second cladding tubes (Komanec, Dousek et al., 2020).

From the timeline of hollow core optical fiber evolution as shown in figure 13, the nested nodeless ARF (figure 13(h)) has been chosen for simulation in this work because it provide the lowest attenuation when comparing with the others.
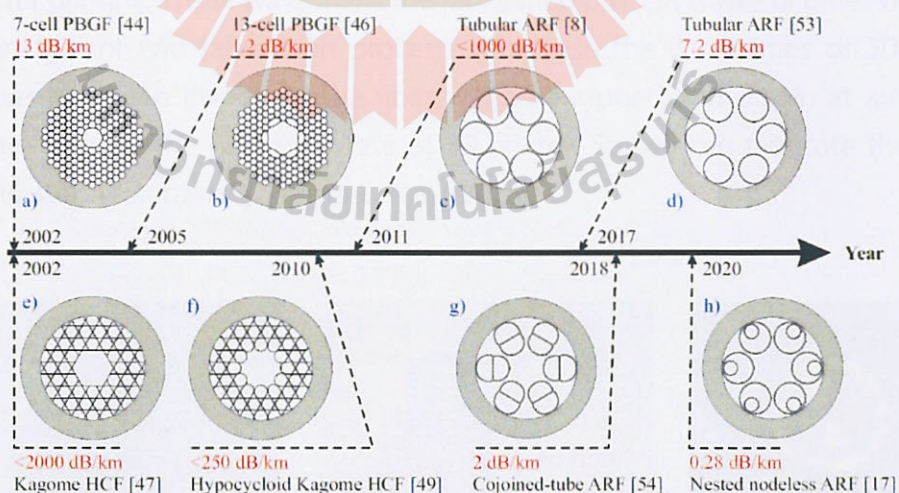
Figure 13 Timeline of the hollow-core optical fiber evolution including both fiber design and attenuation milestones, values are given for the wavelength of 1550 nm. (Komanec, Dousek et al., 2020)

2.2.3 Fabrication of microstructure optical fibers (MOFs)

There are many methods that have been proposed for the fabrication of optical fiber preform with complex structures of the MOFs.

General technique that is used to fabricate the MOF preform is a "stack and drawing" method (Nadella, Spruiell et al,. 1978). By using this technique, the fiber preform will be created by assembling the silica rod with the desire structure inside the tube. This technique can be used to fabricate both solid-core and hollow-core fiber. Another well-known technique is "drilling" (Becker, Werner et al,. 2013). For this technique, the fiber structure preform is created by drilling the glass or polymer rod by using laser or drill. This technique is a fast fiber preform fabrication technique but require a shot length of silica or polymer rod due to the limitation in length of drilling wand. An "billet extrusion" technique is another fiber preform fabrication method which can be done by forcing the liquid polymer or the silica billet through die (Gattass, Rhonehouse et al., 2016).

The new technique to fabricate the MPOF preform is a direct extrusion using 3D printer. This technique has the potential to use as a miniaturized fiber drawing tower. The microstructured polymer optical fibers (MPOFs) can be fabricated in a single step by using this technique.

In the beginning, 3D printing is only used to print the structure of the optical fiber for the preform process (Cruzl, Serrão et al, 2015). The drawing process has been drawn after printing. These ways make the fabrication process waste of time. Therefore, a combination of two fabrication processes that use the capabilities of 3D printing techniques has been invented. The fiber will be extruded and drawn at almost the same time through the heated nozzle of 3D printer. So, we can fabricate the MPOFs in a single step (Talataisong, Ismaeel et al., 2018).
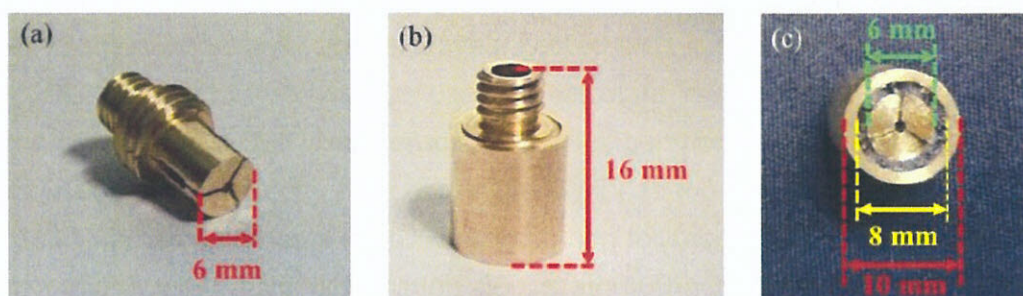
Figure 14 Nozzle for extrude the MPOFs. (a) Nozzle body, (b) Nozzle body + cover, (c) after MPOF drawing. (Talataisong, Ismaeel et al., 2018)
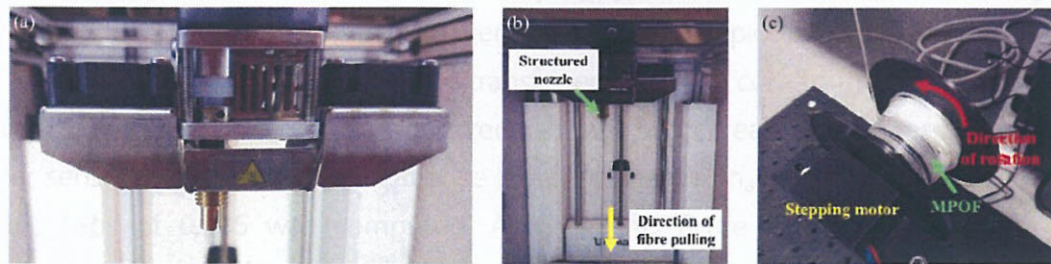
Figure 15 Set up for drawing the MPOFs from 3D printer. (a) Nozzle connected with the heater of 3D printer. (b) Fiber pulling from the heated nozzle. (c) MPOF wrapped onto the spool connected to the stepper motor. (Talataisong, Ismaeel et al., 2018)

The design of the nozzle of 3D printer (figure 14) can be flexible designed and created based on the desired structure of the optical fiber. To fabricate the MPOF by using the direct-extrusion technique, the structured nozzle will be connected to the heater head of 3D printer (figure 15(a)), then material will be fed through the heated structure nozzle. The extruded material will be pulled to create the MPOFS with the desired fiber dimension (figure 15(b)) by using the rolling spool as shown in figure 15(c). (Talataisong, Ismaeel et al., 2018)

2.2.4 Simulation structure of MOFs

A computer simulation is a way to show how a real-world system or process works overtime. For the optical fiber, our interesting fiber structure will be mimicked in simulation software like COMSOL and Lumerical to predict the guided mode that confines the fiber core and others. The detail below will discuss some examples of the MOFs simulation paper.

In 2016, Xianchao Yang et al. used surface plasmon resonance and birefringence to analyze a graphene-based photonic crystal fiber (PCF) sensor as presented in figure 16. The sensor's cladding of the fiber design in this work including two layers of air holes which hexagonal arranged around a central air-core. The bigger holes in the second layer are selectively coated with graphene-Ag bimetallic layers. COMSOL Multiphysics software is used to calculate guided mode using the finite element method (FEM). The sensor section is partitioned into several triangular subdomains using perfectly matched layers (PML) as the boundary condition. There are 183,578 mesh elements in all. The simulation for modal analysis is carried out in the XY plane while light propagation occurs along the Z-direction, as illustrated in figure 17. The 2D and 3D electric field distributions of the designed fiber sensor at resonance wavelength = 590 nm are shown in figure 17(a). Due to its asymmetrical

construction and the fact that light mainly propagates in the Y-direction, this designed fiber structure exhibits strong birefringence. As clearly depicted in figure 17(b), when SPR takes place, some energy will be transferred from the core to the metal-dielectric contact and the intensity of the reflected light will be decreased. To assess the optical fiber sensor's performance, a refractive index of analyte (n_a) ranges from 1.33 to 1.35 with steps of 0.005 was computed. According to figure 18, as n_a increases, the resonance peak shifts to a longer wavelength and the peak loss increases. After optimizing d_2/Λ, d_c/Λ, the thickness of the Ag layer, and the number of the graphene layer, the wavelength sensitivity is as high as 2520 nm/RIU with a resolution of 3.97 × 10^{-5} RIU (Yang, Lu et al., 2017).
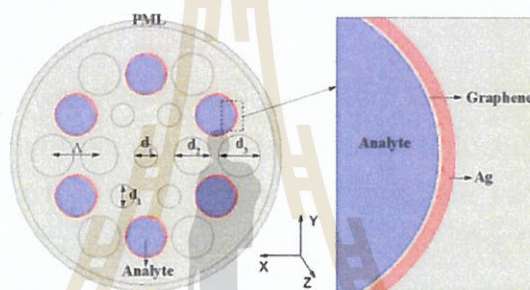
Figure 16 Schematic of the designed fiber sensor. (Yang, Lu et al., 2017)
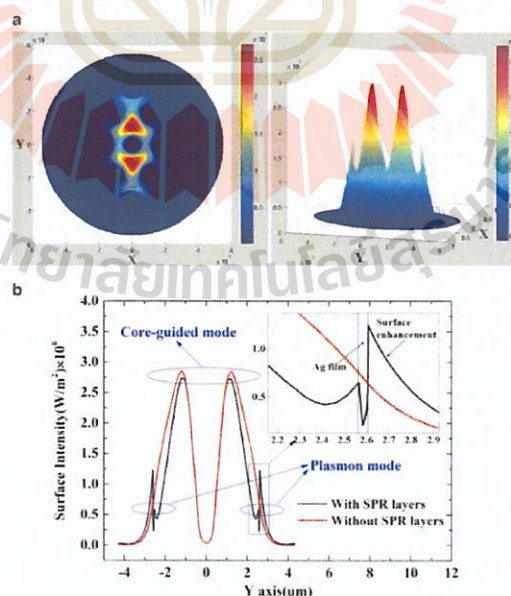
Figure 17 (a) 2-D and 3-D electric field distributions of the fundamental mode at resonance wavelength λ = 590 nm. (b) Electric field intensity distribution at the middle of the sensor along the y-axis at resonance wavelength λ = 590 nm. (Yang, Lu et al., 2017)
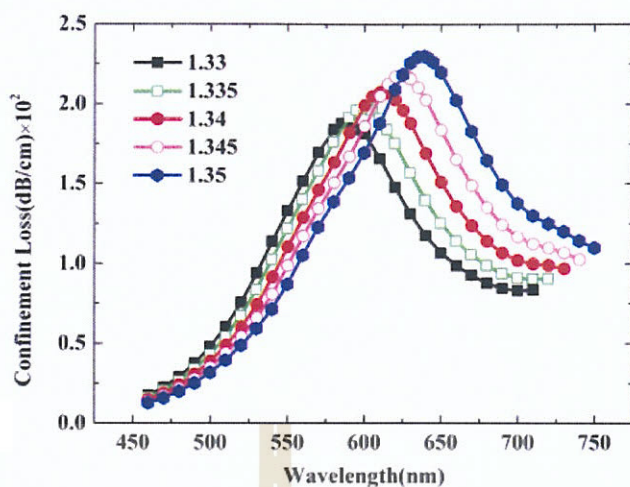
Figure 18 Loss spectra of the designed sensor when n_a varies from 1.33 to 1.35 with the steps of 0.005. (Yang, Lu et al., 2017)

The fiber design with four rings of the square, circular, and hexagonal photonic crystal fiber (PCF) geometry are presented in (Hossain, Bulbul et al,. 2017) as illustrated in figure 19. This fiber has been designed to evaluate various optical properties throughout a wavelength range of 800 nm to 1600 nm. The three types of geometry have been used to analyze the effective area, propagation constant, confinement loss, and waveguide dispersion. The silica was chosen to be the background material, and the cladding region is constructed from four air-hole layers. In COMSOL software, a perfectly matched layer (PML) absorbing boundary condition is applied in the outer layer after the air hole layers. The simulation result from COMSOL provides the complex effective refractive index of the guided mode in optical fiber. According to the numerical analysis, the effective area is found to be large for square PCF geometry and small for hexagonal PCF geometry (11.827 μm^2, 10.588 μm^2, and 9.405 μm^2, for square, circular, and hexagonal PCF geometry respectively). The results of the analysis, all three PCF structures achieve approximately zero waveguide dispersion between 900 and 1500 nm and approximately zero confinement loss at wavelength ranges between 800 and 1250 nm. Once more, a circular PCF structure at 900 nm achieves negative dispersion of about 30.354 ps/(nm•km).
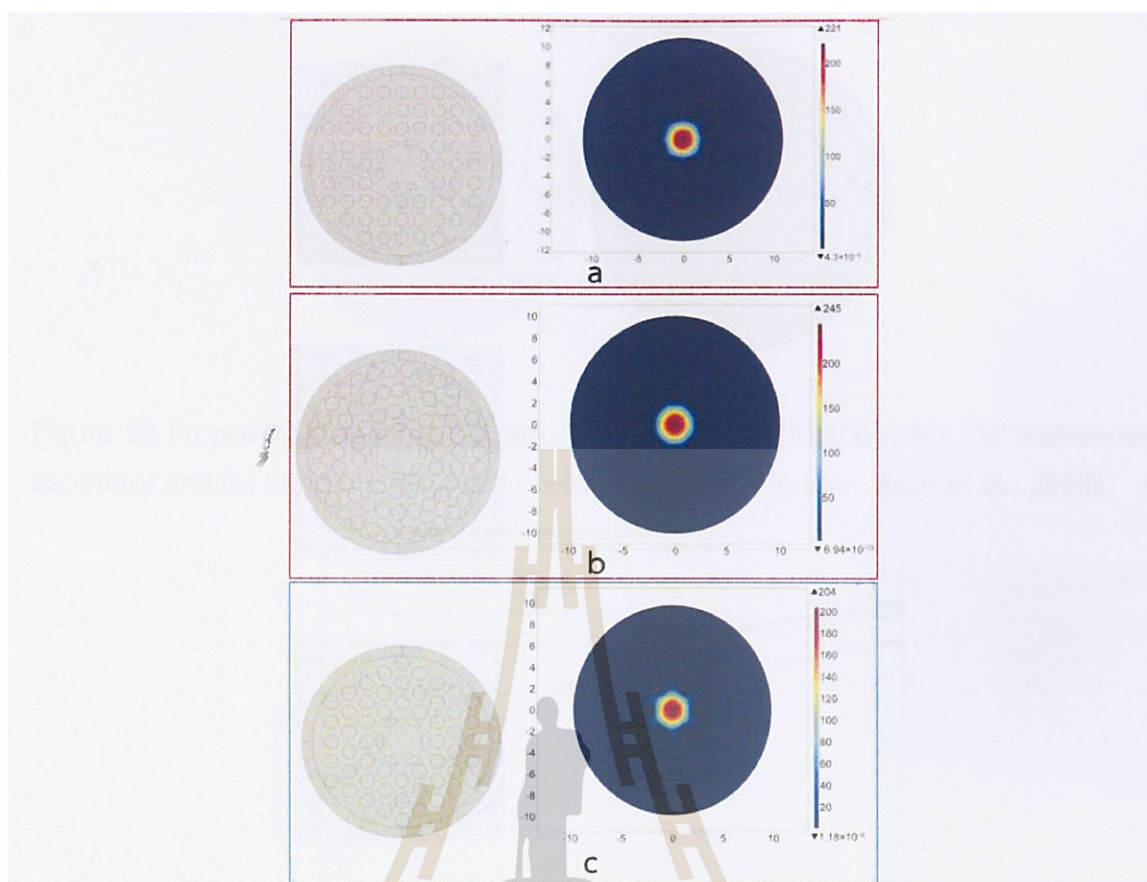
Figure 19 Transverse geometry, and fundamental mode field of the Square (a), Circular (b) and Hexagonal (c) PCF geometry. (Hossain, Bulbul et al., 2017)

An analysis of the relative sensitivity profile of alcohol through the PCF at various temperatures was presented by Etu Podder et al. in 2018. Figure 20 shows the hexagonal PCF structure that was used in this work. The COMSOL multiphysics software was used to simulate the optical mode in the hexagonal PCF structure. The material is silica glass, which is surrounded by three layers of air holes. Different of ethyl alcohol concentrations are used to fill 6 holes and another 7 holes in the core area at different temperatures (20°C, 25°C and 30°C). The simulation method is carried out at the 600–1600 nm wavelength range. A perfectly matched layer (PML) with the thickness of 0.7 μm is used as a boundary for the simulation. The concentration and operating temperature of the ethyl alcohol-water mixture affect the mixture's refractive index. The relative sensitivity of the designed fiber with different alcohol percentage is presented in figure 21. The relative sensitivity increases when ethyl alcohol concentration is increased and also with the increasing of the operating wavelength (Podder, Jibon et al., 2018).
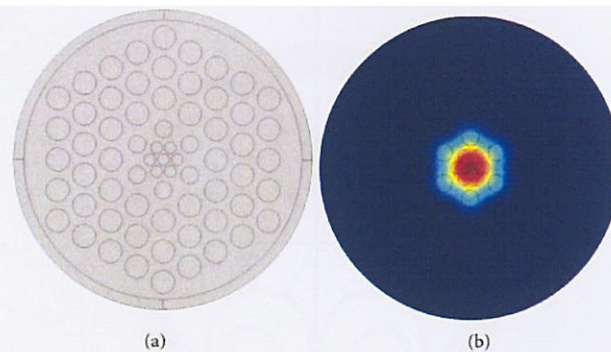
Figure 20 Proposed hexagonal PCF structure in COMSOL Multiphysics: (a) Transverse geometry and (b) Fundamental mode field of the PCF. (Podder, Jibon et al., 2018)
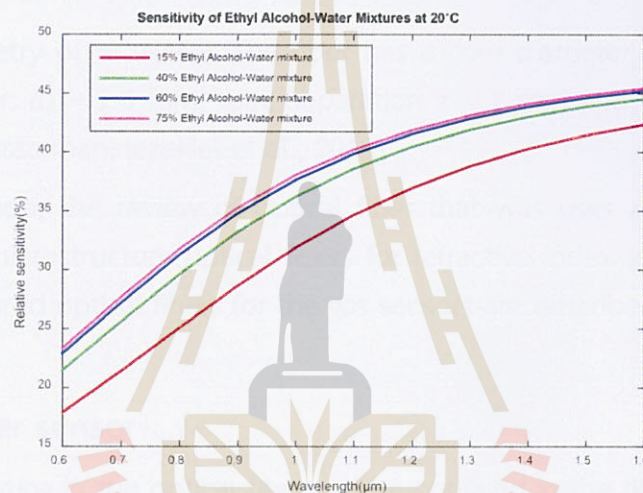
Figure 21 The sensitivity profile of Ethyl Alcohol water mixture for different concentration at temperature 20˚C. (Podder, Jibon et al., 2018)

In 2018, a hollow-core nested anti-resonant node free fiber (HC-NANF) with low transmission losses is proposed for broadband THz guiding. The geometry of the proposed HC-NANF is shown in figure 22. COMSOL software, which is based on the finite element method (FEM), was used to carry out the numerical simulations. A perfectly matched layer (PML) was imposed in the structure's outermost region as a boundary of the simulation. Extremely fine meshes with maximum element sizes of $\lambda/4$ and $\lambda/6$ in the air and material regions, respectively, were used in the simulation for an accurate simulating result. After optimized core diameter (D_C), Outer capillary external diameter (d_o), tube thickness (t), and tube separation (z) at operating wavelength 1 THz, the structure has D_C = 3 mm, d_o = 2.6 mm, t = 0.09 mm, and z = 1 mm. And according to numerical simulation, the low loss of 0.05 dB/m with a dispersion-flattened bandwidth at 0.6 THz is achieved (Hasanuzzaman, Iezekiel et al., 2018).
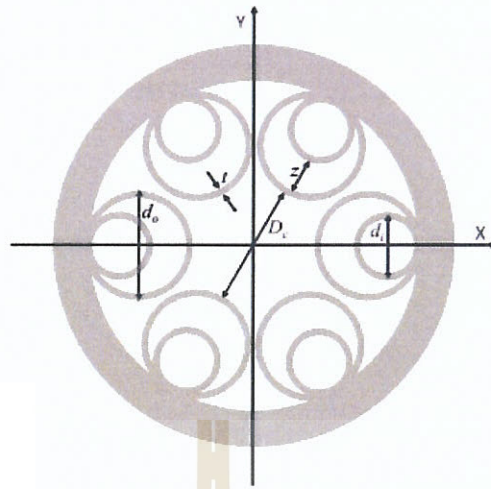
Figure 22 Geometry of HC-NANF. The fiber has a core diameter D_C = 3 mm, outer capillary diameter, d_o = 2.6 mm, tube separation z = 1 mm and tube thickness, t = 0.09 mm. (Hasanuzzaman, Iezekiel et al., 2018)

Next section, the review of optical fiber that was uses as a sensor will be presented. The microstructure optical fibers for refractive index sensors, and hollow core microstructured optical fibers for the gas sensors are described below.

2.3 Optical fiber sensor

Light propagating in the optical fiber will be confined in the fiber core while part of it can be penetrated to the cladding region. The penetration of light from the fiber core to the cladding can be explained as an evanescent wave which will be rapid decayed in amplitude with increasing distance from the core. The penetration depth (d_p) is given by (Lu, Chen et al., 2008)

$$d_p = \frac{\lambda}{2\pi(n_1{}^2 sin\theta^2 - n_2{}^2)^{\frac{1}{2}}} \quad . \tag{9}$$

where λ is the wavelength of light propagate in the optical fiber, n_1 is the refractive index of the core, n_2 is the refractive index of the cladding, and θ is the incident angle.
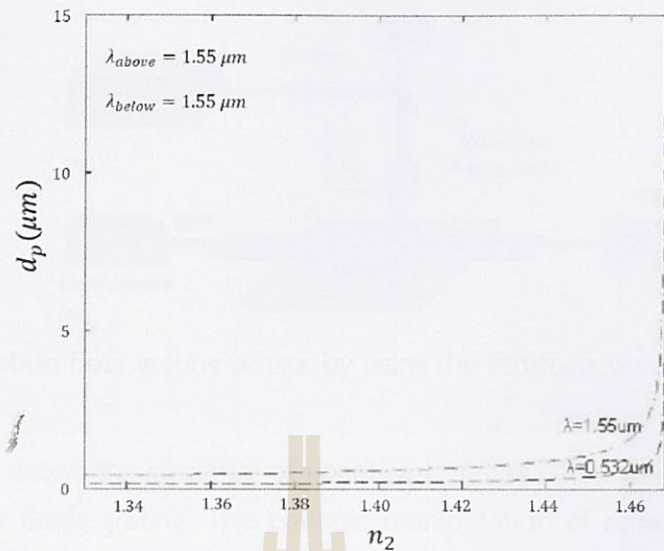
Figure 23 The penetration depth (d_p) compare with the refractive index of the cladding (n_2) at the wavelength (λ) 1.55 and 0.532 um. (Lu, Chen et al., 2008)

Figure 23 shows that the penetration depth (d_p) will be increased with the increasing of the refractive index of the cladding (n_2) and the wavelength light guided in the fiber core. In optical fiber sensor technology, the structure of the fiber core and the cladding will be modified to increase the interaction of evanescent wave for sensing target.

2.3.1 Fabrications of Optical Fiber Sensors

- Grating Inscription

Fiber grating is one of the fiber structures that is used for the sensing application including the fiber Bragg grating and long period fiber grating. The fiber Bragg grating (FBGs) can be fabricated by using many techniques such as the phase mask technique and the laser inscription. For the laser inscription technique so call point-by-point technique, many types of lasers were used, such as an ultraviolet laser, but this laser is restricted to the photosensitive fibers. Thus, the grating inscription by using the femtosecond laser is more famously use. Figure 24 shows, the inscription on the core of the single-mode fiber to manipulate the periodic change in the fiber core by using the femtosecond laser. The femtosecond laser can be used with a non- photosensitive fiber and can be used to inscribe the fiber core without stripping the outer coating. (Joe, Yun et al., 2018)
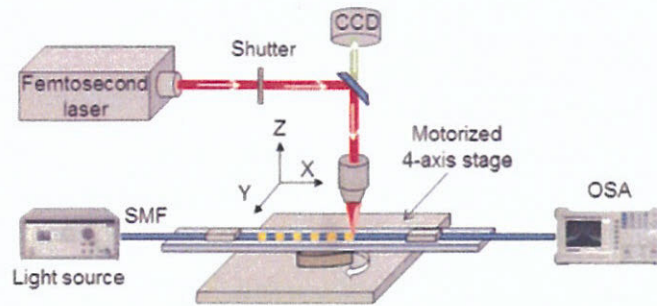
Figure 24 Frabication fiber grating sensor by using the femtosecond laser. (Joe, Yun et al., 2018)

Figure 25 shows the structure of fiber Bragg grating. The top figure indicates the structure of fiber Bragg grating. The periodic manipulation of refractive index in the fiber core is presented in the middle figure, including the high (n_3) and low (n_2) index. The figure at the bottom reveals the spectrum of the input, transmitted, and reflected signal. By launching the broadband light source into the fiber Bragg grating, the transmission spectrum shows that only a specific wavelength will not be able to pass through the fiber. On the other hand, the reflection spectrum shows the peak of the high reflected wavelength. This reflected wavelength calls the Bragg wavelength (λ_B) which is defined as:

$$\lambda_B = 2n_{eff}\Lambda. \tag{10}$$

where Λ is the periodicity of the gratings, and n_{eff} is the effective refractive index of the grating.
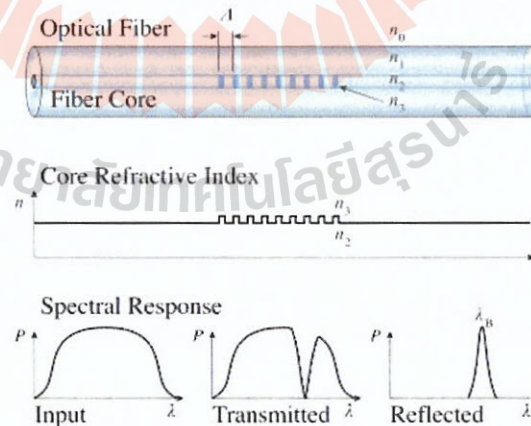
Figure 25 The fiber bragg grating structure, with refractive index profile and spectral response.

● Optical Fiber Shaping

For fabricating the optical fiber sensor, shape and structure of the optical fiber can be modified to increase the interaction of the evanescent field with the sensing target. Many methods for shaping the optical fiber have been developed, consisting of the direct machining, tapering, side-polishing, and splicing techniques. Three methods to modify the shape of the original shape of the optical fiber are shown in figure 26.

The direct machining is a technique, which is, used the focused ion beam (FIB) to inscribe the outer layer of fiber as presented in figure 26(a). The Focused Ion Beam (FIB) is an optical instrument that focuses and scans an accelerated ion beam on a sample to locally sputter the material surface to directly fabricate arbitrary nanostructures (Joe, Yun et al., 2018).

The tapering method uses to changes the cladding and the core diameter of the optical fiber (Joe, Yun et al,. 2018). Fiber taper can be created by heating and the axial force pulling the fiber at the same time, as shown in figure 26(b).

The side-polishing method shown in figure 26(c) is the fundamental idea to polish the optical fiber. The leaking light at the polish surface can interact with the surrounding materials directly (Joe, Yun et al., 2018).
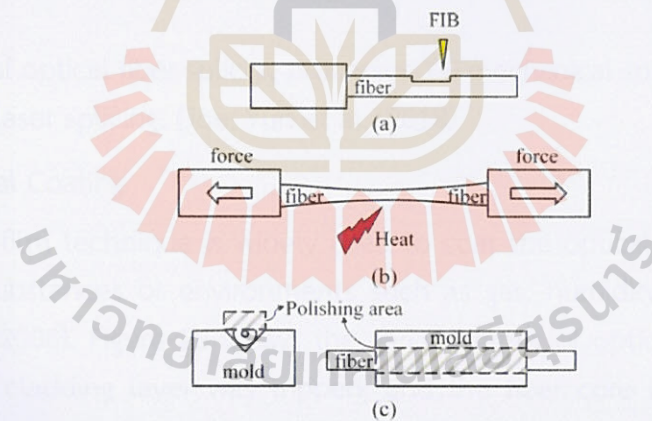
Figure 26 Type of optical fiber shaping processes: (a) direct machining, (b) tapering, and (c) side-polishing. (Joe, Yun et al., 2018)

Apart from these three methods which are used to shape the optical fiber structure, the splicing method is also used for this proposal (Joe, Yun et al., 2018). The spliced approach is a method for connecting two optical fibers. It is not a technology that directly modifies fiber structure to be a sensor, but it is commonly used for splicing to a standard fiber that acts as a lead-in/lead-out fiber for the optical fiber sensor or connect 2 optical fiber sensors together. Figure 27 shows three basic methods to modify the optical fiber structure by using the splicing technique. Figure 27(a), the

mechanical splicing uses the mechanical device to grip two fibers together. It is a simplest method but has a high transmission loss. In figure 27(b), the fusion splicing is used to splice two fibers together by using high heat from an electric arc. Fusion splicing has transmission loss lower than mechanical splicing and widely used because of its fast and cost-effective technique. Figure 27(c) shows the splicing technique by using the CO_2 laser. The laser splicing gives a high resolution to increase heating position control. It can be used to connect two different fibers, such as single-mode fiber (SMF) with different core diameters, single-mode fiber (SMF) and multimode fiber (MMF), and single-mode fiber (SMF) and photonic crystal fiber (PCF).
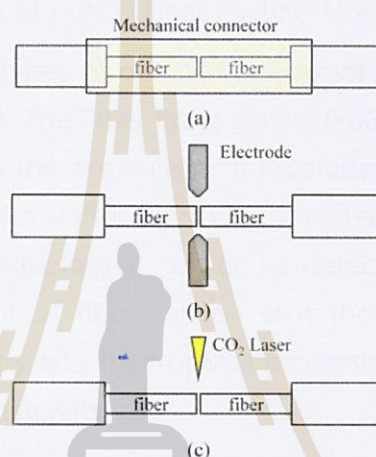
Figure 27 Type of optical fiber splicing processes: (a) mechanical splicing, (b) Arc fusion splicing, and (c) laser splicing. (Joe, Yun et al., 2018)

- Functional Coating

The thin-film technique is widely used to coat the optical fiber for detecting some specific substances or environments such as gas, humidity, and pH (Richter, Paschew et al,. 2008). Figure 28 shows the various types of optical fiber coating. In figure 28(a) the cladding layer was tripped, and the fiber core is coated with the substance of interested, which is called the etched optical fiber technique. The coated tapered optical fiber is presented in figure 28(b), the optical fiber was tapered before coating. The side-polishing as presented in figure 28 (c) is another technique to remove the cladding of the optical fiber before coating with the selective material. In general, coatings are used as a selective material to adjust the selectivity or sensitivity of the optical fiber sensors (OFS). Those functional coatings alter the optical property of the propagating cladding mode so that the OFS becomes more sensitive. The metal oxide sensing layer, and bio-recognition elements has been widely studied for optical fiber coating. (Joe, Yun et al., 2018)
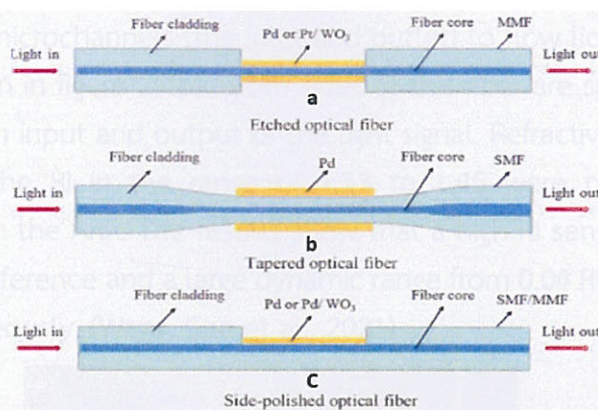
Figure 28 Various types of optical fiber coating. (Joe, Yun et al., 2018)

The various fabrication types of optical fiber sensors as presented above can apply to many types of sensors. The Fiber Bragg grating (FBG) can apply as a pressure and temperature sensor, when the pressure or temperature change the Fiber Bragg grating will change leading to the shift in the Bragg wavelength. Optical fiber coating can apply as a chemical and biological sensor to detect specific chemicals and biomolecules. The tapered optical fiber can be sent the evanescent field to the surrounding environment directly and their optical properties will show us about the properties of the surrounding materials.

There is the modification of optical structure fiber that not only can be used in sensing application but also have the optical fiber that suitable for sensor application without destroying the form of the fiber. It is called microstructured optical fibers (MOFs). This type of fiber is different from the fiber sensor described previously as they do not require the increasing of the evanescence field in the cladding region to interact with the detecting analyte, but the interaction of light can be occurred inside the MOFs due to their intrinsic air-holes.

The MOFs can be used as a gas medium to flow the ethylene into the holes inside the fiber structure. the change of the ethylene concentration causes the change of its refractive index. These changes can be detected by monitoring the change of optical properties of light guiding in the optical fiber So, in the following section, the review of MOFs for a refractive index sensor and gas sensors will be presented.

2.3.2 Microstructure optical fibers (MOFs) refractive index (RI) sensor

The refractive index (RI) sensor based on microstructure optical fiber (MOFs) are usually used in chemical and biological application. The intrinsic air-holes in this structure allow liquid or gas to flow in which is suitable for biological or chemical sensing. For example, the structure of hollow core antiresonance fiber (ARF) was drilled

to connect with two microchannels (the inlet and outlet) to flow liquid into the fiber cladding ring, as shown in figure 29(b). Both sides of this fiber are spliced with single mode fiber (SMF) as an input and output of the light signal. Refractive index matching liquids (RIMLs) with the RI in the range of 1.33 to 1.45 were pumped into the microfluidic channel in the ARF. The results show that a high RI sensitivity of 19014.4 nm/RIU for mode interference and a large dynamic range from 0.04 RIU for ARROW can be achieved simultaneously. (Wang, Gao et al., 2021)
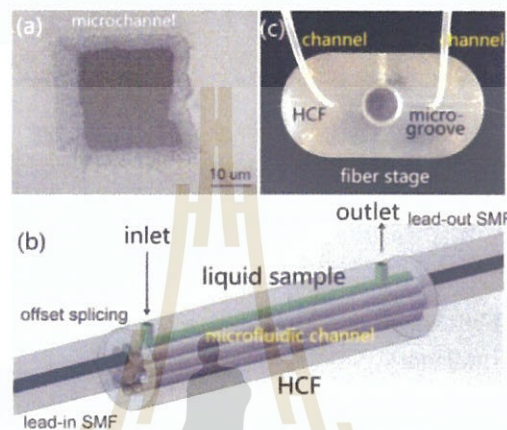
Figure 29 (a) Microchannel in the HCF; (b) schematic of in-line microfluidic channel in the HCF ; (c) fiber stage. (Wang, Gao et al., 2021)

For another example, in 2008, the 24 mm-long large-mode-area photonic crystal fiber (PCF) was spliced with the SMF as shown in figure 30. The oils with different RI from 1.33–1.44 ranges were dropped on the PCF surface near the splice area. The result shows that, at the high index range of 1.38–1.44, a maximum resolution of 2.9×10^{-4} RIU was found, while at indices in the 1.33–1.38 range the resolution was 2×10^{-3} RIU. (Silva, Roriz et al., 2014)
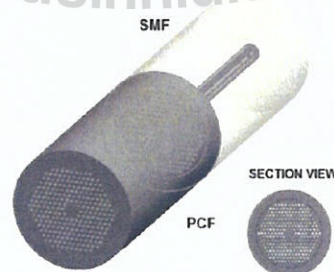
Figure 30 Sensing head designed for refractive index (RI) sensing using a fiber probe based on a large-mode area photonic crystal fiber (PCF) and detail of the PCF cross-section view. (Silva, Roriz et al., 2014)

Table 2 Overview of the various types of MOF-based refractometers developed for liquid RI sensing and according RI sensitivity and/or resolution results. (Silva, Roriz et al., 2014)

Structure device	RI Range	RI Sensitivity	Resolution (RIU)
Fiber tip	1.38–1.44		2.9×10^{-4}
SMF/ large-mode area PCF	1.33–1.38	-	2×10^{-3}
Fabry-Perot fiber tip SMF/endlessly single mode PCF/SMF	1.32–1.44	4.59/RI	2×10^{-5}
Fabry-Perot fiber tip SMF/ PCF/SMF	1.332–1.427	–11.27/RIU (Fast Fourier Transform)	2×10^{-4}
Directional coupler architecture using a solid-core PCF	1.50 @ 25°C	38,000 nm/RIU @ 52°C	$4.6 \times 10{-7}$
Interferometric fiber tip PCF/coreless silica fiber	1.410–1.430	850 nm/RIU	-
SMF/Hollow-core PCF/SMF	1.35–1.39	24.5 nm/RIU	8.1×10^{-4}
	1.39–1.43	46.5 nm/RIU	4.3×10^{-4}
SMF/large-core air-clad PCF/SMF	1.3196–1.3171	800 nm/RIU	3.4×10^{-5}
Dual-core PCF (microstructured and solid cores)	1.33	8500 nm/RIU	2.02×10^{-6}

Table 2 (Continued) Overview of the various types of MOF-based refractometers developed for liquid RI sensing and according RI sensitivity and/or resolution results. (Silva, Roriz et al., 2014)

Structure device	RI Range	RI Sensitivity	Resolution (RIU)
Intermodal PCF interferometer	1.340 1.360	70 µW/RIU 679 W/RIU	1.5×10^{-5}
Dual-core MOF (Ge-doped and side-hole cores)	1.5–1.66	3259 nm/RIU (TM01) 3183 nm/RIU (TE01) 2956 nm/RIU (HE21)	-
Microcell based on an endless single-mode PCF	1.3	9100 nm/RIU	-
Two-core chirped MOF	1.42	300/RIU	3×10^{-6}
SPR-based solid-core gold-coated honeycomb PCF	1.33	2800 nm/RIU	3.6×10^{-5}
LPG written in a large-mode area PCF	1.33	1500 nm/RIU	2×10^{-5}
LPG written in an endlessly single mode PCF filled with water	1.33–1.35	-	4.42×10^{-7}
SPR-based on a PCF with a central air hole coated with gold	1.37–1.41	5500 nm/RIU	10^{-6}
SPR-based on a gold-coated wagon wheel MOF	1.33–1.36	-	6.5×10^{-6}

Table 2 (Continued) Overview of the various types of MOF-based refractometers developed for liquid RI sensing and according RI sensitivity and/or resolution results. (Silva, Roriz et al., 2014)

Structure device	RI Range	RI Sensitivity	Resolution (RIU)
Rounded tip-based PCF	1.337–1.395	262.28 nm/RIU	-
FBG written in a MOF	1.4–1.44	15, 21 and 45 nm/RIU	2.2 to 6.7 $\times$ 10^{-5}
SPR-based grapefruit PCF filled with different numbers of silver nanowires	1.33–1.335	2400 nm/RIU	4.51 $\times$ 10^{-5}
SPR-based on a closed-form multi-core holey fiber	1.33–1.42	2929.39 nm/RIU	-
SMF/tapered-PCF/SMF	1.43–1.53 1.33–1.34	9231.27 nm/RIU 1629 nm/RIU	-
Etched two-core MOF	1.3160–1.3943	3119 nm/RIU	-
FBG written in exposed-core MOF	1.3–1.4	1.1 nm/RIU	-

2.3.3 Hollow core microstructure optical fibers (HC-MOFs) gas sensor

In sensing applications, the solid-core photonic crystal fiber is mostly used as a physical sensor, such as displacement, pressure, and temperature. While gas sensors can be made from either solid-core or hollow-core fiber. In this work, only the hollow-core antiresonance fiber (ARF) has been considered. Its structure is suitable for designing the guided wavelength to correspond with the absorption band of flowing gas or liquid inside the fiber air-holes. The wavelength shift is probably how we find the sensitivity of our gas with ARF characteristics. In addition, compared to other forms of microstructured hollow-core fibers, ARF will not be complicated for future fabrication. The table below shows various hollow-core fiber-based gas sensors. (Yu, Chen et al., 2020)

Comparison of performance indicators for different HC-PCF gas sensors.

Table 3 Comparison of performance indicators for different HC-PCF gas sensors.

Gas	Wavelength	Sensing Principle	Type of fiber/Length	Response or Averaging Time/Assisted Pressure	Detection limit
Acetylene (C_2H_2)	1510-1540 nm	DAS[1]	HC-PBGF/5 m	240 s/0.7 bar	Not stated
	1528.03 nm	DAS	HC-PBGF/2 m	Sub minute/<1 bar	<100 ppm
	1500-1550 nm	DAS	HC-PBGF/0.33 m	several minutes/several bar	Not stated
	1530.1–1530.7 nm	WMS[2]	HC-PBGF/13 m	Not stated	<1 ppm
	1530.371 nm	PTS[3]	HC-PBGF/0.62 m	Not stated	2 ppb
	1510–1545 nm	DAS	Suspended ring-core PCF/0.25 m	8.7 min/0.5 bar	Not stated
	1532.83 nm	WMS	HC-PBGF/0.094 m	Not stated	7 ppm
	1514–1538 nm	DAS	HC-PBGF/1 m	4 s/113 mbar	Not stated
	1518.71 nm	DAS	HC-PBGF/0.9 m	20 min/0.1 bar	500 ppm
	1315–1345 nm	DAS	HC-PBGF/1 m	4 s/113 mbar	Not stated

Table 3 (Continued) Comparison of performance indicators for different HC-PCF gas sensors.

Gas	Wavelength	Sensing Principle	Type of fiber/Length	Response or Averaging Time/Assisted Pressure	Detection limit
Methane (CH_4)	~1666 nm	WMS	HC-PBGF/0.137 m	248 s/not stated	158 ppm
	1665.48 nm	DAS	HC-PBGF/ 0.07 m	3 s/ 0.1 bar	647 ppm
	3.19–3.36 μm	FTS[4]	HC-PBGF/0.8 m	2 min/2 bar	50 ppm
	3.33 μm	WMS	HC-ARF/1.3 m	<10 s/1.1 bar	Single ppm
	3.33 μm	CLDS[5]	HC-ARF/1.3 m	1 s/1.1 bar	500 ppb
Ammonia (NH_3)	1500 nm	DAS	HC-PBGF/1 m	4 s/113 mbar	Not stated
	1531.7 nm	DAS	HC-PBGF/1 m	Not stated	20 ppm
Nitrogen (N_2)	584.5 nm	SRCS[6]	HC-PBGF/1.5 m	36 s/6.9 bar	Not stated
	313–833 nm	RCS[7]	HC-PBGF/0.3 m	10 s/not stated	Not stated
Oxygen (O_2)	559 nm	SRCS	HC-PBGF/1.5 m	36 s/6.9 bar	Not stated
	313–833 nm	RCS	HC-PBGF/ 0.3 m	10 s/not stated	Not stated
Propane (C_3H_8)	535–545 nm, 600–610 nm	SRCS	HC-PBGF/1.5 m	36 s/6.9 bar	Not stated
Ethane (C_2H_6)	535–545 nm, 600–610 nm	SRCS	HC-PBGF/1.5 m	36 s/6.9 bar	Not stated
Carbon dioxide (CO_2)	417–714 nm	RCS	HC-PBGF/0.3 m	3 min/not stated	400 ppm
Toluene (C_7H_8)	313–1000 nm	RCS	HC-PBGF/0.3 m	10 s/not stated	400 ppm

Table 3 (Continued) Comparison of performance indicators for different HC-PCF gas sensors.

Gas	Wavelength	Sensing Principle	Type of fiber/Length	Response or Averaging Time/Assisted Pressure	Detection limit
Acetone (C_3H_6O)	313–455 nm	RCS	HC-PBGF/0.3 m	10 s/not stated	100 ppm
1,1,1-trichloroethene ($1,1,1-C_2H_3Cl_3$)	313–455 nm	RCS	HC-PBGF/0.3 m	60 s/not stated	12000 ppm
Hydrogen cyanide (HCN)	1530–1542 nm	DAS	HC-PBGF/1 m	4 s/113 mbar	Not stated
Hydrogen (H_2)	1532.2 nm	SRGS[8]	HC-PBGF/15 m	250 s/1.6 bar	17 ppm
Carbon monoxide (CO)	2.3 μm	WMS	HC-ARF/0.85 m	5 s/1.8 bar	0.4 ppm
Nitrous oxide (NO_2)	3.6 μm	DAS	HC-ARF/1.2 m	Not stated	35 ppm
	4.53 μm	WMS	HC-ARF/3.2 m	23 s/0.94 bar	Single ppb

1 DAS: direct absorption spectroscopy; 2 WMS: wavelength modulation spectroscopy; 3 PTS: photothermal spectroscopy; 4 FTS: Fourier transform spectroscopy; 5 CLDS: chirped laser dispersion spectroscopy; 6 SRCS: spontaneous Raman scattering spectroscopy; 7 RCS: Raman scattering spectroscopy; 8 SRGS: stimulated Raman gain spectroscopy. (Yu, Chen et al., 2020)

As shown in table 3, there is no report of the use of HC-ARF for ethylene detection at the wavelength of 3.2 μm. Thus, the study of ethylene detection by using the HC-ARF is of interest. In next chapter, the method for the research of HC-ARF design and optimization will be described.

CHAPTER III

MATERIALS AND METHODS

3.1 Mode field distribution

Mode field distribution is the dimension of beam propagates along in longitudinal direction in the optical fiber core. To model the light propagation in optical fiber, we started with the Maxwell's equation.

$$\nabla \times \vec{E} = -\frac{\partial \vec{B}}{\partial t} \; , \tag{11}$$

$$\nabla \times \vec{H} = \vec{J} + \frac{\partial \vec{D}}{\partial t} \; , \tag{12}$$

$$\nabla \cdot \vec{D} = \rho \; , \tag{13}$$

$$\nabla \cdot \vec{B} = 0 \; . \tag{14}$$

where E is the electric field, H the magnetic field, D the electric displacement field, B the magnetic flux density, J, the current density vector, and ρ, the free charge density, represent the sources for the electric field. The electric displacement field and magnetic flux density are related to E and H were given by the following constitutive relations:

$$\vec{D} = \varepsilon_0 \vec{E} + \vec{P} \; , \tag{15}$$

$$\vec{B} = \mu_0 \vec{H} + \vec{M} \; . \tag{16}$$

where P and M are the polarization field and magnetization field, ε_0 the vacuum permittivity and μ_0 the vacuum permeability. An optical fiber is a medium without free chargers, meaning that J and ρ will both equal zero. An optical fiber is also a nonmagnetic medium, so M = 0. This means that the Maxwell equations can be rewritten to:

$$\nabla \times \vec{E} = -\mu_0 \frac{\partial \vec{H}}{\partial t} \; , \tag{17}$$

$$\nabla \times \vec{H} = \varepsilon_0 \frac{\partial \vec{E}}{\partial t} + \frac{\partial \vec{P}}{\partial t} \; , \tag{18}$$

$$\nabla \cdot (\varepsilon_0 \vec{E} + \vec{P}) = 0 \; , \tag{19}$$

$$\nabla \cdot \vec{H} = 0 \; . \tag{20}$$

To describe the wave propagation in optical fiber, the above equation can be used to find the wave equation below:

$$\nabla \times \nabla \times \vec{E} = -\frac{1}{c^2}\frac{\partial^2 \vec{E}}{\partial t^2} - \frac{1}{\mu_0}\frac{\partial^2 \vec{P}}{\partial t^2} \ . \tag{21}$$

Most of the optical fiber are fabricated from a dielectric material that frees electric charges and current sources. So, the Maxwell equations can be manipulated assuming time-harmonic solutions to give the wave equation describing the light propagating in a fiber:

$$\nabla \times \frac{1}{\mu_r}\nabla \times \vec{E} - k_0^2 \varepsilon_r \vec{E} = 0 \ , \tag{22}$$

where k_o, the wave number, and ε_r, the relative permittivity, are defined as:

$$k_o = \frac{2\pi f_0}{c} = \frac{2\pi}{\lambda} \ , \tag{23}$$

$$\varepsilon_r = (n - ik)^2 \ , \tag{24}$$

where n is the real part of the refractive index, k the imaginary part of the refractive index, f_0 the frequency, λ the wavelength and c the speed of light.

To find a solution for equation (22), the boundary conditions that depends on materials in our geometry we added need to be considered. For antiresonance fibers (ARFs) in this work, two materials including air-core and polymer (PET) for tube in cladding structure will be added in the simulation. With no surface charges and surface currents, therefore, the boundary conditions below must be satisfied:

$$n \times \left(\vec{E}_1 - \vec{E}_2\right) = 0 \ , \tag{25}$$

$$n \times \left(\vec{H}_1 - \vec{H}_2\right) = 0 \ , \tag{26}$$

$$n \cdot \left(\vec{B}_1 - \vec{B}_2\right) = 0 \ , \tag{27}$$

$$n \cdot \left(\vec{D}_1 - \vec{D}_2\right) = 0 \ , \tag{28}$$

From equations (25) and (26), on this boundary, the tangential component of the electric and magnetic field must be continuous. From equations (27) and (28), the normal component of the magnetic flux density and the electric flux density must also be continuous, and the normal component of the magnetic field is also continuous for non-magnetic media. However, the normal component of the electric field is not continuous on the boundary between two media.

Because of the complexity of the refractive index distribution in ARFs, analytical solutions for equations (22), (25), (26), (27), and (28) won't be able to obtain. It is however known that the field will be time-harmonic. Because the waveguides studied

in this work are longitudinally invariant, the field can be considered as shown in equation (29) as described by Bloch's theorem.

$$\vec{E} = A(x,y) \times e^{i\beta z} \, . \tag{29}$$

where A is the transverse amplitude, and β the propagation constant along the z-axis, defined as $\beta = n_{eff} + ik_z$. The wave equation can be considered an eigenvalue problem by using the boundary condition. Its eigenvectors are the mode field distributions, where from its eigenvalues one can obtain β. Subsequently, the loss for a modeled fiber can be determined from the imaginary component of the propagation constant. (Putten, 2019)

3.2 Research procedure

3.2.1 COMSOL Multiphysics software

To design the structure of hollow-core fiber with anti-resonant tube, COMSOL Multiphysics software was used to fine an electric field distribution of EM-wave via Maxwell's equations by using finite element method (FEM) technique. Therefore, the studying the COMSOL Multiphysics software is important for this research. COMSOL Multiphysics software is a simulation platform that encompasses all the steps in the modeling workflow, from defining geometries, material properties, and the physics that describe specific phenomena to solve and post-processing models for producing accurate and trustworthy results.
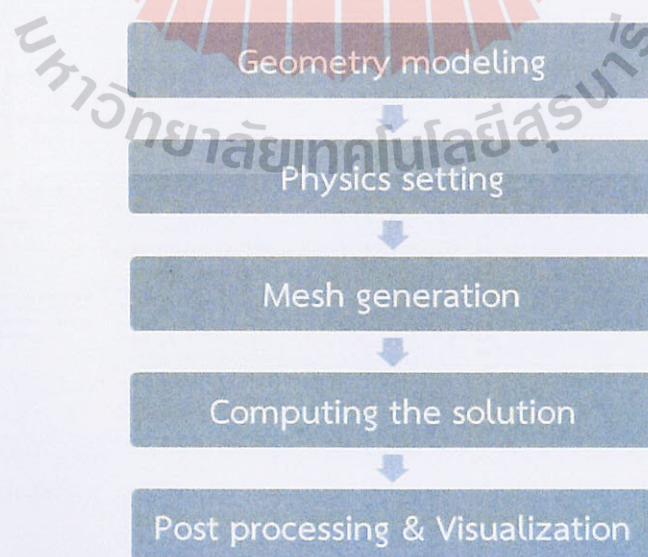
Figure 31 Flowchart for Modeling.

Figure 31 shows the flowchart for the modeling of the hollow-core anti-resonant fiber using COMSOL. The simulation will be divided into 5 steps which will be started with a geometry modeling based on our interested optical fiber structure. The next step is to identify the physics settings, followed by the mesh generation. Then, the solution of the question will be computed. Finally, the results are explained using post-processing and visualization tools. (Castrellon-Uribe, 2012)

In the initial simulation in COMSOL software, the physics (figure 32(a)) for the optical simulation design was selected. Then, the program will show the model builder window (figure 32(b)) consisting of the model builder, setting, and graphics part. The result of the simulation after setting the parameter value will be shown on the graphics part.

(a)

(b)

Figure 32 COMSOL MUTIPHYSICS software user interface (UI) window.

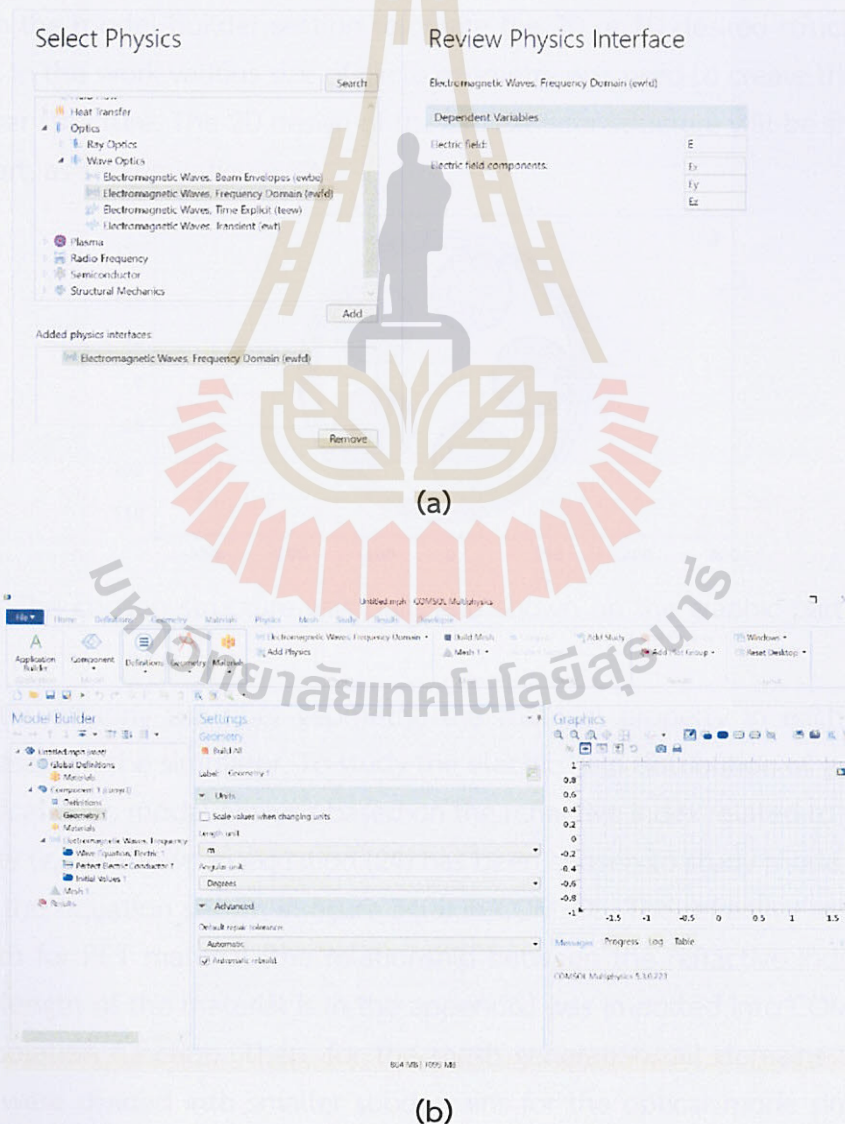For the modeling, the fiber structure as shown in figure 35(a) was built in COMSOL. This fiber structure has been chosen for this project because it is the structure (nested HC-ARF structure) that has been reported as the HC-ARF with lowest confinement loss (Komanec, Dousek et al., 2020). This project aims for the modal simulation the light guiding in the HC-ARF and the calculation of the confinement loss to optimize the structure for wavelength of 3.2 μm in which related to the ethylene absorption wavelength. Before processing the geometry modeling, the parameter, and the value of each variable, such as the operating wavelength, frequency, and fiber diameter, were added in the global definition, as shown in the model builder part of figure 32(b). These parameters will be applied to the entire model.

As shown in figure 32(b), the geometric shapes such as triangles and circles can be built in the model builder section to create the 2D or 3D desired structure for the simulator. In this work various size of circle geometry was used to create the proposed optical fiber structure. The 2D design of the optical fiber structure will be shown in the graphic part, as shown in figure 33.
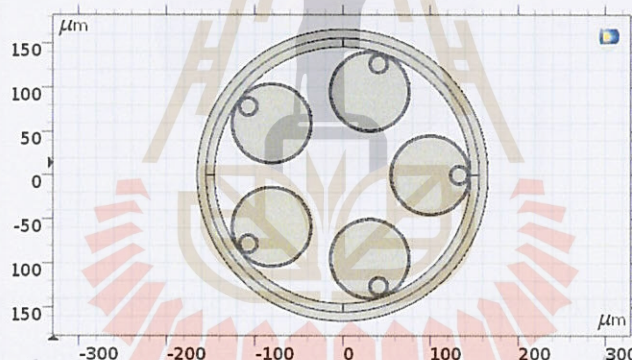
Figure 33 The chosen structure was built and shown on the graphic part window in COMSOL.

After creating the fiber geometry, the material property in each domain is defined based on the simulator. To study the electric field distribution of guided mode in the optical fiber, modal analysis based on the refractive index related to the relative permittivity (ε_r) as shown in equation (24) has been chosen to study mode analysis by following the equation shown in figure 34(a) in COMSOL. The refractive index of each wavelength for PET material (the relationship between the refractive index with the and wavelength of the material is in the appendix) was imported into COMSOL by via the interpolation function. Then, for the mesh generation, all domains in our fiber structure were divided into smaller subdomains for the optical mode simulation by using the finite element method (FEM).

After all parameters for the simulation have been set, the software will be able to solve the Maxwell's equation as shown in equation (22). After solving the process, the result of the electric field distribution of the guided mode in the optical fiber following equation (29) will show in the graphic window as shown in figure 34(b).

Show equation assuming:

Study 2, Mode Analysis

$$\nabla \times (\nabla \times E) - k_0^2 \epsilon_r E = 0$$

$$\lambda = -j\beta - \delta_z$$

$$E(x,y,z) = \bar{E}(x,y)e^{-ik_z z}$$

(a)

(b)
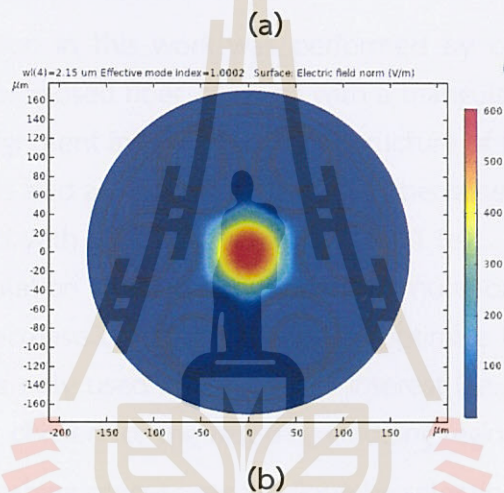
Figure 34 (a) Mode analysis setting in COMSOL. (b) The graphic window shows the electric field distribution of the mode guide in the fiber after solving.

3.2.2 Finite elements method (FEM)

The finite elements method (FEM) is a numerical method used in COMSOL multiphysics software for solving differential equations in engineering and mathematical modeling. FEM solved Maxwell's equation with boundary conditions in this project by managing the equation into the generalized eigenvalue problem, where constant propagation β is the eigenvalue and the electrics fields are eigenvectors. To do the FEM, all domains in the fiber structure were meshed into smaller sub-domain as shown in figure 35(b), and the solution is founded in each sub-domain by solving for the eigenvalues. The fundamental mode is founded in the fiber core after simulation proceed as shown in figure 35(c).

Figure 35 (a) Fiber structure; (b) Triangular mesh used in fiber structure; (c) Fundamental mode found in fiber structure.
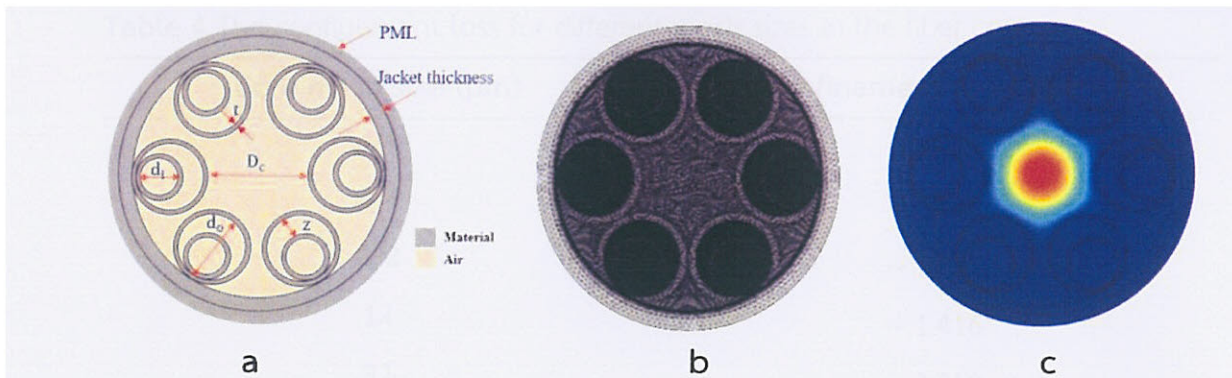
Modal simulation in this work was performed by creating the 2D structure (cross-section) of the proposed fiber. Meshing with a triangular shape was chosen due to its best structure alignment inside the circular structure of the optical fiber. The size of the mesh element is also an important parameter because the accuracy of the FEM solution can be varied with the mesh size. The small (e.g., Less than λ) mesh sizes provide accurate simulation results. However, the simulation time will be increased drastically with the decrease of the mesh size. To optimize the calculation time, the smaller mesh size was only used in the area of interest (i.e., fiber core region) and a coarser mesh size was chosen for the rest (i.e., cladding region).

In COMSOL, meshing process can be done by selecting the mesh size provided by the software such as course, fine, finer or generate a custom mesh manually. Mesh size can be adjusted via a physics-controlled or user-controlled mesh sequence type, accordingly. In this work, the mesh sizes in each domain in the simulation area are manually defined by using user-controlled mesh. Table shows the confinement loss affected by the mesh size in the fiber core. The mesh size of 5 times of the wavelength (5λ) is coarse and providing a high confinement loss. The confinement loss is dramatically decrease when the mesh size is changed from 3λ to λ. Until mesh size is less than or equal to $\lambda/2$, confinement loss is not fluctuated with the change of mesh size. Therefore, with the limit of simulation time, the mesh size of the core equal to $\lambda/4$ has been chosen while the mesh size in the cladding area is fixed to λ.

Table 4 The confinement loss for different mesh sizes in the fiber core.

Core mesh size (μm)	Confinement loss (dB/m)
$\lambda/6$	~ 1.083
$\lambda/4$	~ 1.080
$\lambda/2$	~ 1.078
1λ	~ 1.416
3λ	~ 7.519
5λ	~ 7.538

The boundary condition at the outer layer of the simulating area is also an important parameter for an accuracy of the simulation result. Using the finite element approach to solve Maxwell's equation requires a modeling domain of finite size, as well as a set of boundary conditions. In the COMSOL simulation environment, there are 2 available boundary conditions including the scattering boundary condition (SBC), and the perfectly matched layer (PML).

Scattering boundary condition (SBC) is used to avoid back reflection of the outgoing wave from the exterior boundary of your computational domain. In another words, this boundary condition makes a boundary transparent for the outgoing waves. The perfectly matched layer (PML) is a domain or layer that is added to an acoustic model in order to simulate an open and non-reflective infinite domain. As an alternative to nonreflective boundary conditions, it creates a domain with perfect absorption. Figure 36 shows the reflection from a PML with respect to incident angle as compared to the SBCs. The outcome indicates that the PML reflects the smallest amount throughout the broadest range. As the wave propagates almost perfectly parallel to the boundary, reflection still occurs.
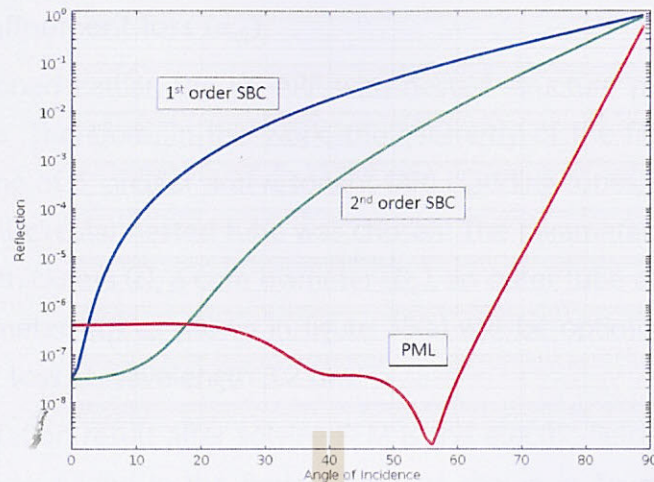
Figure 36 Reflection of a plane wave at the first- and second-order SBC and the PML with respect to angle of incidence. (Frei, 2015)

Therefore, to mimic the environment surrounding the real fiber, the artificial absorbing layer known as the perfect match layer (PML) as shown in figure 35(a) is used in this work for solving the electromagnetic wave equation. PML is very important for calculating the leakage loss of fiber. Without the PML, the light would reflect into the fiber instead of leaking away, which would lead to an incorrectly calculated leakage loss for the structure.

After selecting the type of boundary condition, the PML thickness is varied as shows in figure 37. The result showing that the fluctuation of the confinement loss is very small (<0.002 dB/m) with the variation of the PML thickness. . It indicates that the guide mode at this operating wavelength is completely confine within the fiber core. As the simulation time will be increase with an increasing the PML thickness, therefore, the PML thickness of 14 μm was chosen to reduce the simulation time.
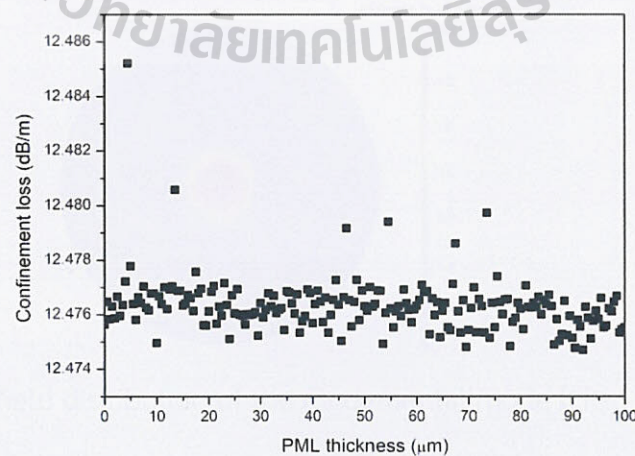

Figure 37 Confinement loss as a function of PML thickness from 0-100 μm, sweep step 0.5 μm at operating wavelength 3.2 μm.

3.2.3 Confinement loss (α_{cl})

As mentioned earlier, the HC-ARF with nested structure provides the lowest confinement loss. Therefore, in this work, the geometry of the fiber starts from the cladding consisting of 6 circular anti-resonant (AR) cladding tubes, and each AR tube containing a small circular nested tube was chosen. The parameters in fiber geometry including a tube thickness (t), a core diameter (D_c), an outer tube diameter (d_o), and a nested tube diameter (d_i) as shown in figure 35(a) will be optimized to achieve the low confinement loss at wavelength 3.2 μm.

The simulation result after solving FEM is the electric field distribution of the fundamental mode guided in the hollow core, as shown in figure 38. Even though COMSOL can simulate the fundamental mode and higher-order modes, we only considered the confinement loss of the fundamental mode in this work. Because, as illustrated in figure 39, the higher-order mode has a substantial energy loss into the cladding region and showing a higher confinement loss. In practical applications, a single mode guidance is required to store the most energy in the fiber core. In this study, we evaluated only the fundamental mode losses.

After solving, we can obtain real and imaginary parts of the effective refractive index between the fiber core and cladding from COMSOL for calculating the confinement loss, following this equation, (Hasanuzzaman, Iezekiel et al., 2018)

$$\alpha_{cl} = 8.686 \left(\frac{2\pi f}{c}\right) Im(n_{eff}) \tag{30}$$

where α_{cl} is the confinement loss (dB/m), f is operating frequency, c is the speed of light, and $Im(n_{eff})$ is imaginary part of the effective refractive index.
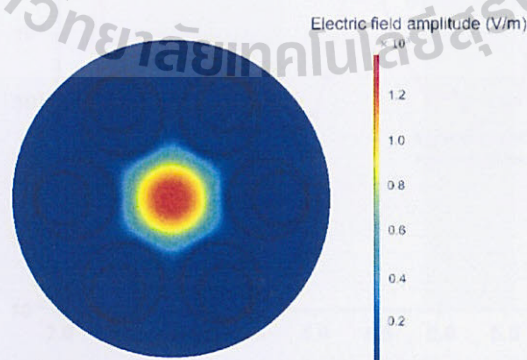

Figure 38 Electric field distribution of the fundamental mode (LP$_{01}$) guided in the core.
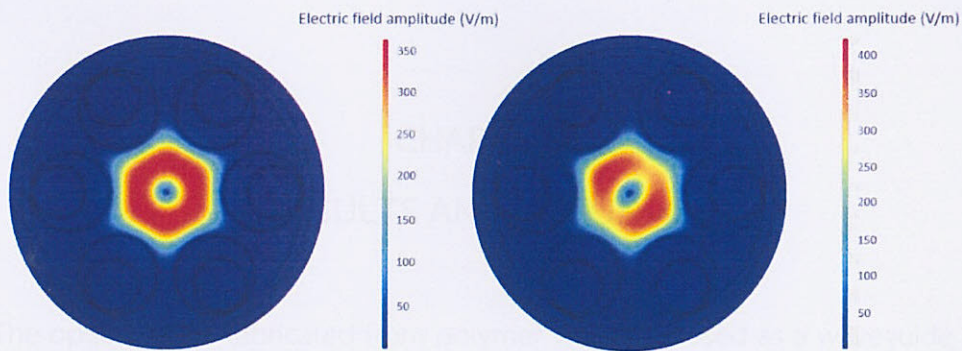
Figure 39 Electric field distribution of the higher order modes (LP_{11}) guided in the core.

At the same operating wavelength, the fundamental mode always has lower confinement loss than the higher-order mode. Such as, the fundamental mode in figure 38 has a confinement loss equal to 1.08 dB/m, while the higher order modes in figure 39 have confinement losses equal to 3.25 and 2.73 dB/m, respectively, at operating wavelength 3.2 µm.

After calculating the confinement loss, all data have been plotted in the OriginPro software for the result analyzation.

Figure 40 shows a graph of confinement loss as a function of wavelength of 2.0–6.0 µm. This graph shows that in this wavelength range, we can see the resonance wavelength at 2.3 and 4.3 µm that has a high loss and the antiresonant wavelength between 2.6-4.0 and 4.9-5.6 µm that has the low loss, as shown in the green band, that has a low loss area.
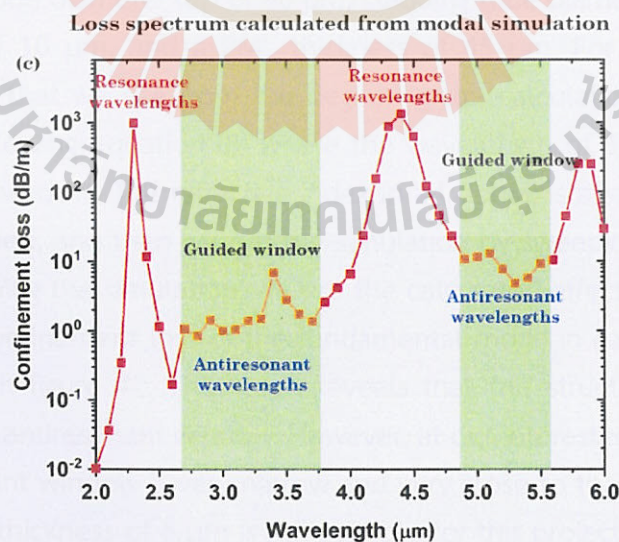

Figure 40 Example of all data plotted in OriginPro for post processing process.

CHAPTER IV

RESULTS AND DISCUSSION

The optical fibers fabricated from polymer were proposed as a waveguide due to their low cost, widely accessible materials, and low-temperature processing. However, most polymers have high material absorption, especially in mid-infrared (mid-IR) region. This high absorption leading to high losses in solid-core polymer waveguides. To overcome this issues, hollow-core fiber has been proposed: since the guided mode of light is mostly confined in a hollow air-core, thus, the effect of material absorption is minimal. In this chapter, the design and structure optimization of hollow core microstructured polymer optical fiber based on antiresonant guidance will be presented.

Initially, the simulation was started by creating a fiber model in COMSOL by referring to the sizes of inner tubes and outer tubes for all the structures from the literature review presented so far that had an inner nested tube with roughly half the diameter of the external one ($d_i/d_o \approx 0.5$) (Poletti, 2014). As shown in figure 41, our first fiber structure has an overall fiber diameter of 405 µm, hollow core diameter (D_c) of 145 µm, inner tube diameter (d_i) of 80 µm, cladding tube diameter (d_o) of 125 µm, jacket thickness of 10 µm, and a PML thickness of 45 µm. For the cladding tube thickness of 6 µm that we use from the beginning the calculation of antiresonance wavelength by following equation (8) where the wavelength of 3.2 µm is located in the antiresonant window. The refractive index in all domains after creating the fiber structure were added, and then we run the simulation by sweeping wavelength from 2 to 12 µm. Following the simulation, we use the calculated effective refractive index to calculate the confinement loss of the fundamental mode in each wavelength and the result shows in figure 42. This result reveals that this structure can signify the resonant peak and antiresonant window. However, at our interested wavelength of 3.2 µm, the antiresonant window is very narrow and very close to the resonant peak. So, the cladding tube thickness of 6 µm is not suitable for this project. Moreover, hollow core diameter (D_c) of 145 µm is too large, causing to the confinement loss to be affected by a higher order mode and the structure is not symmetric. Therefore, the core diameter of the fiber has been reduced of the fiber and make it symmetric.
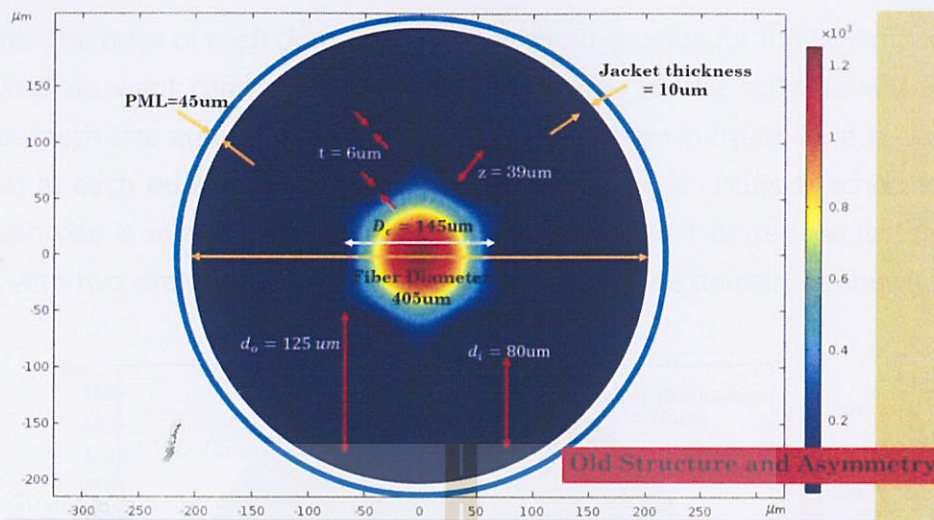
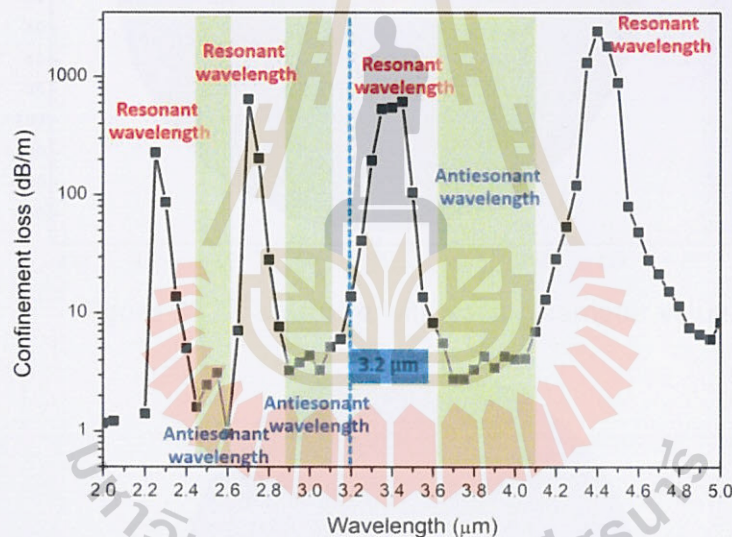Figure 41 Initial structure with each parameter value.

Figure 42 Confinement loss as a function of wavelength of 1st structure at cladding tube thickness is 6 μm.

The second structure has an overall fiber diameter of 312 μm, hollow core diameter (D_c) of 108 μm, inner tube diameter (d_i) of 58 μm, cladding tube diameter (d_o)) of 84 μm, jacket thickness of 10 μm, a PML thickness of 14 μm, and a cladding tube of 4 μm. The nested tube that overlaps the outer tube as shown in figure 43 has been removed. At this core size, we can reduce the effect of higher order mode and ensure that the optical fiber is single mode at an operating wavelength of 3.2 μm. Next, we adjust the fiber structure again because we noticed that the nested tube, cladding tube, and jacket thicknesses are divided into 4 domains in the modeling process. We chose the circle structure with thickness, which is why our mentioned tube has 4

domains. The edge of each domain affects the mesh creation for the FEM process. The mesh size we want cannot be created at that edge. So, the software will generate another mesh size automatically to fit that edge as show in figure 44. It is obvious to see that at each edge of each domain, especially at three circles attached together, the mesh size is smaller than others. Therefore, to make it better, we recreated the model with two circles to make the tube thickness has one domain, as shown in figure 45.

Figure 43 2nd structure with each parameter value.

Figure 44 Mesh size in fiber 2nd structure with four domains in each circle.
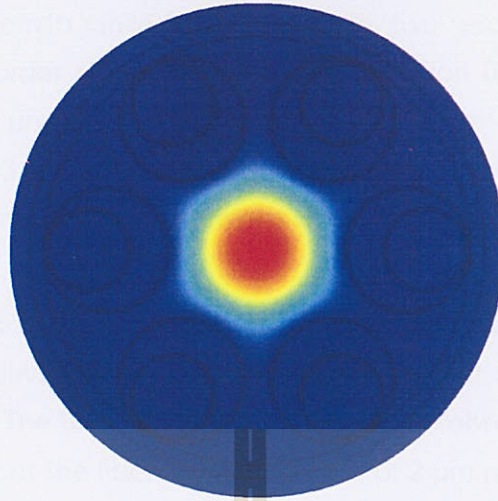
Figure 45 Final structure that we used to optimized parameters.

After getting the final structure, we optimize the mesh size and PML thickness. The outcome is depicted in Chapter III. Other parameter optimization is covered in the section below.

4.1 Structure optimization for 3.2 µm guiding.

The hollow-core antiresonant fiber (HC-ARF) theoretical transmission characteristics were evaluated by using the FEM solver Comsol© mode solution to numerically solve Maxwell's equations in the frequency domain for the electric field. The simulation was performed by creating a 2D model of the fiber cross section structure with the same dimensions as described in chapter III.

4.1.1 Effect of changing of tube thickness (t)

As shown in equation (8), the thickness of the tube (t) determines the position of the high-loss resonance wavelength and the low-loss antiresonance window. Thus, the modal simulation by varying the tube thickness was first performed to find an optimal thickness of tubes where the antiresonant window is located at a wavelength of 3.2 µm. As we mentioned at the beginning of this chapter, the tube thickness of 6 µm is not suitable for this work, and a thickness thicker than 6 µm is unnecessarily thick, which can cause a higher loss due to the material absorption. So, the simulation with the variation of tube thickness in this research was focused on the tube thickness of 1–5. The simulation results for each thickness are discussed further below.

Figure 46 shows the confinement loss as a function of wavelength for different tube thicknesses of 1.0, 2.0, 3.0, 4.0, and 5.0 µm. Variations of tube thickness in the cladding affected the position of the resonant wavelengths. The results in figure 46

show that in the wavelength range from 2.5-4.5 μm, two resonant wavelength peaks, which are a different order of resonance (m) in equation (8), can be observed for thicknesses of 4 and 5 μm. Only one resonance wavelength peak can be seen with the thickness of 2 and 3 μm while there is no resonance wavelength in this range at thicknesses of 1 μm. Thus, the antiresonance window covers the wavelength range of 2.5-4.5 μm.

Figure 46 shows that the lowest loss and broadest window of antiresonance wavelength can be achieved at the thickness of 1.0 μm, but this thickness is too thin for fabrication process. The low loss window can also be observed at the thicknesses of 2.0, 4.0, and 5.0 μm but the fiber with a thickness of 2 μm provides a broader valley than the other two thicknesses. At a thickness of 3 μm, resonance wavelength (high loss) is located at a wavelength close to 3.2 μm. Therefore, a tube thickness of 2 μm was selected against the other thicknesses for the simulation.
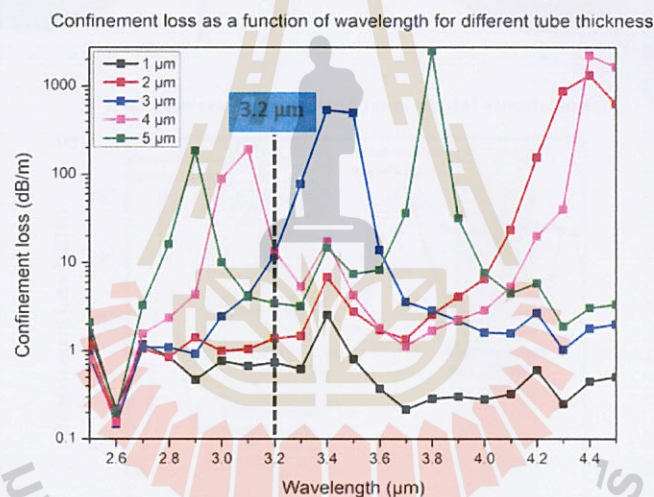

Figure 46 Confinement loss as a function of wavelength for different tube thicknesses t with D_c = 128 μm, d_o = 92 μm, and d_i = 62 μm.

By using the formula in equation (8), the resonant wavelengths in the range of interest (2 - 6 μm) when the thickness of tube is 2 μm are calculated to be λ_m = 4.6, 2.3, 1.5, 1.1, 0.9 μm. The modal analysis of the HC-ARF structure (figure 47(a)) shows that at the resonant wavelength (4.6 μm), the field is poorly confined in the central air core, and the mode in the fiber core is coupling with the surrounding material and leaks out to the cladding, resulting in high loss. Figure 47(b) shows that at the antiresonant wavelength (3.2 μm) the field is well confined in the central air core.

The FEM calculated loss spectra are shown in figure 47(c): the peaks of high loss are located at the resonant wavelengths, which correspond to the calculated

resonant frequencies. The loss profile in figure 47(c) shows that specific mid-IR wavelength regions in the range = 2 – 6 μm experience the antiresonance effect. The chosen HC-ARF geometry should effectively guide the wavelength of 3.2 μm at the tube thickness of 2 μm and the resonant peaks (where losses are high) are clearly defined. As expected, field confinement becomes stronger as the wavelength decreases because the core size is relatively larger compared to the wavelength. This confirms that most of the power is confined within the central air core.
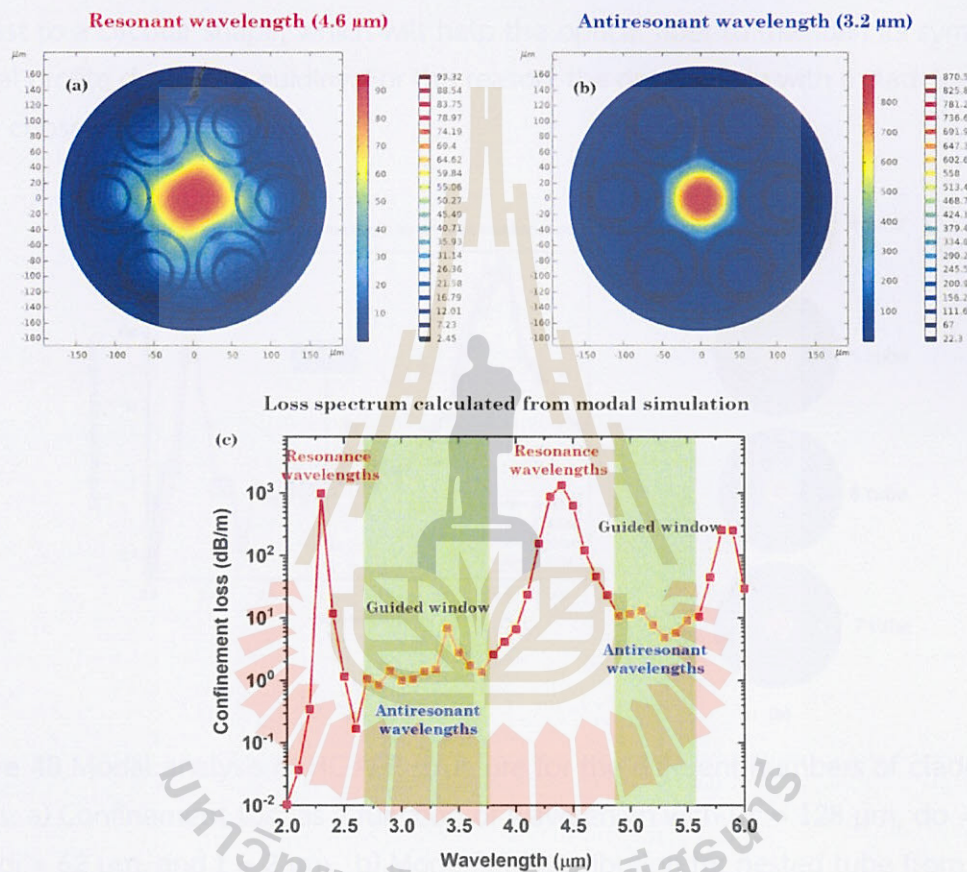

Figure 47 Modal analysis of HC-ARF structure; a) Mode field distribution at resonant wavelength, b) Mode field distribution at antiresonant wavelength, c) Loss spectrum calculated from modal simulation.

4.1.2 Number of cladding tubes

After varying the thickness of the cladding tube, the thickness of 2 μm was chosen. Next, number of cladding tubes was considered to find an effect of number of cladding tubes with the confinement loss and the literature review in chapter 2 reported that the HC-ARF with 6 cladding tubes have the lowest loss nowadays. Therefore, to find an optimal number of cladding tubes where the number of cladding

tubes and confinement loss at the wavelength of 3.2 μm is lowest, the modal simulation when the cladding tubes are varied from 4–7 is examined.

Figure 48 shows confinement loss as a function of wavelength for a different number of cladding tubes. The result shows that the confinement loss at a wavelength of 3.2 μm is not obviously different from the variation of cladding tubes. In the simulation, we were looking for the smallest number of cladding tubes for the fabrication proposed such that the shape of the mode guided in the fiber core was closest to a circular shape, which will help the optical fiber to maintain its symmetric modal profile during the guiding. For this reason, the optical fiber with 6 cladding tubes were chosen.
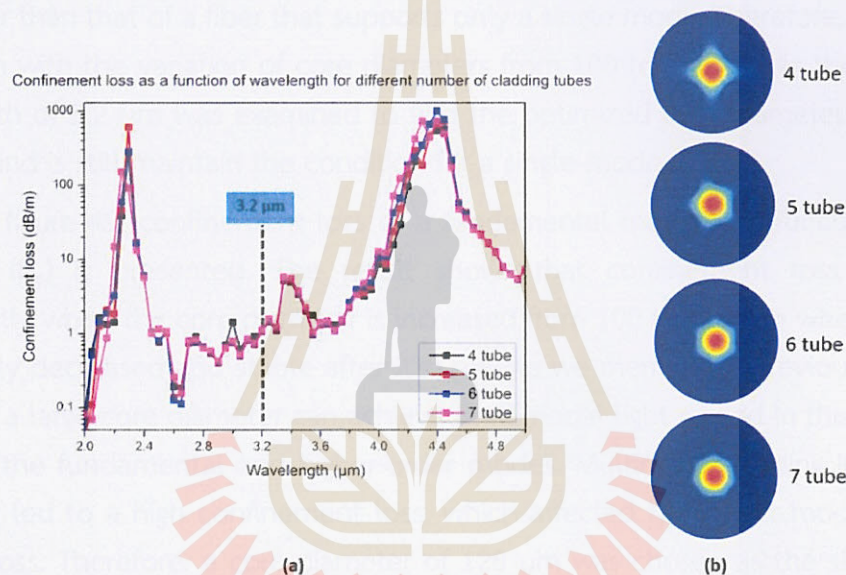

Figure 48 Modal analysis of HC-ARF structure for the different numbers of cladding tubes; a) Confinement loss as a function of wavelength with Dc = 128 μm, do = 92 μm, di = 62 μm, and t = 2 μm., b) Mode field distribution for nested tube from 4-7.

4.1.3 Effect of core diameter (D_c) with loss

The core diameter of the fiber is another parameter that can affect the confinement loss of the guided light inside the fiber core. The guiding principle of the HC-ARF is that the wall of the cladding tubes behaves as the Fabry-Perot etalon, as presented in Chapter III. The treatment of the tube wall as the Fabry-Perot etalon can be done when the core diameter is infinite. In 2019, Terai (Terai, Kubota et al., 2019) ported that confinement loss of HC-ARF is related to the propagation constant of mode in the radial direction and the fiber core diameter, where the loss will be decreased with an increase in core diameter.

As shown in equation 30, confinement loss depends on the effective refractive index (n_{eff}), whose value is related to the core diameter. When the core is enlarged, consequently prevents light from leaving the core because the mode filed diameter is better confined in the fiber core, and the difference in refractive index between the core and cladding increases. Hence the decreasing of the n_{eff} (Yakasai, Rahman et al., 2018) resulting in a decreasing of the confinement loss. However, as shown in equation A-3 in appendix part, a larger core diameter affects a higher-number of guided modes including the high order modes which can induced a higher loss due to the bending loss. A bigger core diameter causes an increasing of v-number. If the v-number is exceeded 2.4048, it confirms that this fiber is a multimode fiber, which makes the total loss higher than that of a fiber that supports only a single mode. Therefore, the modal simulation with the variation of core diameters from 100 to 360 μm at the operating wavelength of 3.2 μm was examined to find the optimized core diameter that has a low loss and is still maintain the condition for a single-mode fiber.

In figure 49, confinement loss of a fundamental mode as a function of core diameter (D_c) is presented. The result shows that confinement loss decreases dramatically when the core diameter is increased from 100 to 220 μm where the loss is gradually decreased and stable after 220 μm. As we mentioned previously, optical fiber with a large core diameter can achieve multimodal light guided in the fiber core, including the fundamental and higher-order modes. Multimodal guiding in the large core fiber led to a high confinement loss, which affected high-order mode loss and bending loss. Therefore, a core diameter of 128 μm was chosen as the single mode condition still occurs at this core diameter.
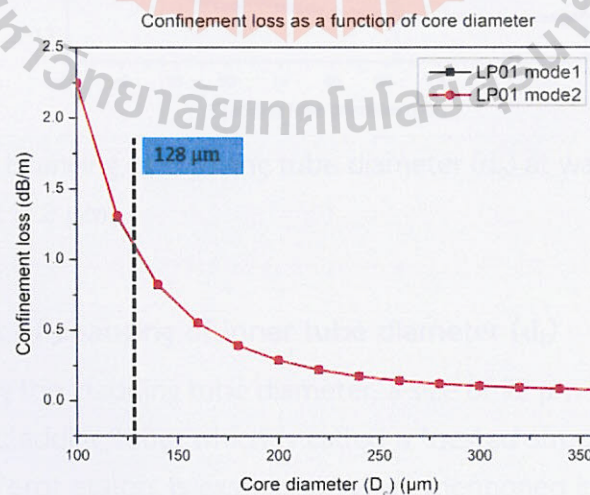

Figure 49 Confinement loss as a function of core diameter (D_c) with d_o = 92 μm, d_i = 62 μm, and t = 2 μm.

4.1.4 Effect of changing the cladding tube diameter (d_o)

After varying the core diameter, a size of 128 μm was chosen. Next, the cladding tube diameter was considered to find the size that makes the optical fiber has a low confinement loss. The cladding tube is one of the parameters that affect confinement loss, as the smaller tubes cannot provide two parallel surfaces for the Fabry-Perot etalon. The cladding tube diameter cannot be too large until all tubes are stick together; otherwise, the material loss would be significant. So, to find the optimized cladding diameter that provides a low loss, the simulation of the cladding tube diameter without the nested tube from 28 to 128 μm is examined. The result is discussed in the paragraph below.

Figure 50 shows that confinement loss decreases gradually with increasing cladding tube diameter (d_o), and then becomes stable at diameters greater than 80 m. Until around 125 μm, confinement loss has trended to increase again because each tube almost touches the other. Therefore, the cladding tube diameter of 92 μm was chosen as it is in the middle range of stability loss.

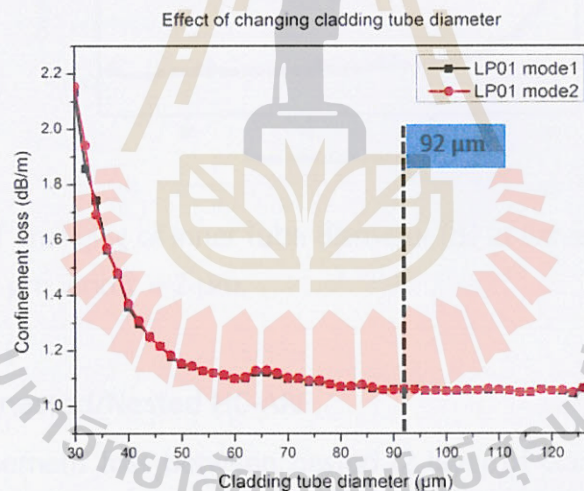**Figure 50** Effect of changing of cladding tube diameter (d_o) at wavelength 3.2 μm with D_c = 128 μm, and t = 2 μm.

4.1.5 Effect of changing of inner tube diameter (d_i)

After varying the cladding tube diameter, a size of 92 μm was chosen. Next, the effect of an inner cladding tube, which is called a "nested structure" that behaves as the second Fabry-Perot etalon, is examined. As we mentioned in the literature review section, the lowest loss structure nowadays has the size of a nested tube around half the length of the cladding tube. It means that the second reflection works best when

the inner tube is half the size of the outer tube (Poletti, 2014). So, in order to find the optimal nested tube diameter that provides a low confinement loss, the modal simulation with the nested tube diameter changing from 6 to 84 µm is examined when the thickness of nested tubes and the number of nested tubes are 2 µm and 6 tubes, respectively. The result is discussed in the paragraph below.

Figure 51 shows that the confinement loss is gradually increases with increasing nested tube diameter (d_i), and suddenly increases due to material absorption as the inner tube diameter approaches (80 µm) the diameter of the cladding tubes. As a result, we can conclude that the inner tube is unnecessary in this project.
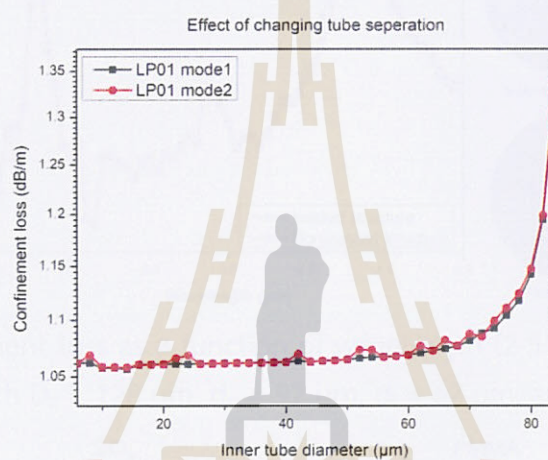

Figure 51 Effect of changing of inner tube diameter (d_i) at wavelength 3.2 µm with Dc = 128µm, do = 92 µm, and t = 2 µm.

4.1.6 Non-nested/Nested HC-ARF

The confinement loss between nested (2 layer of cladding tubes) and non-nested (1 layers of cladding tubes) structures was compared to assess the need for having the nested tube in the fiber structure. The result in figure 52 shows that confinement loss between the two structures is not significantly different at the wavelength of 3.2 µm. Therefore, the non-nested structure has been selected due to the easier fabrication process. Although the nested HC-ARF has been reported as the lowest structure for antiresonance guidance, material absorption is also affected by the total loss of this structure. In this work, polyethylene terephthalate (PET) was used as a fiber, which is a polymer with a hydrocarbon bond, leading to strong adsorption in the mid-IR regime. Thus, the effect of double reflection from the nested tube for the lower loss will not be observed when the material has a high absorption loss at

the operating wavelength. So, from this result, the inner tubes are not needed for the proposed fiber.

The simulation of nested and non-nested structures in other materials is examined to confirm the effect of high material absorption in the mid-IR regime. The result is shown in figure 53. SiO₂ and PMMA (Polymethyl methacrylate) are also not significantly different at the wavelength of 3.2 μm. So, the optimized materials among SiO2, PMMA, and PET are examined and described in the next part.
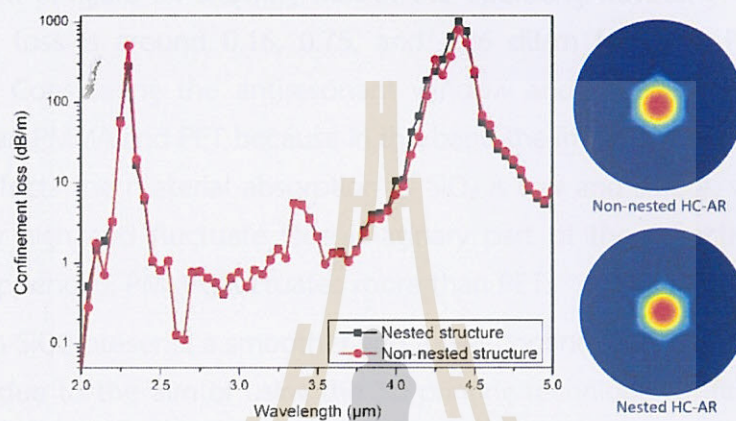

Figure 52 Confinement loss as a function of wavelength (2-5 μm) of non-nested and nested structure with D_c = 128 μm, d_o = 92 μm, d_i = 62 μm, and t = 2 μm.
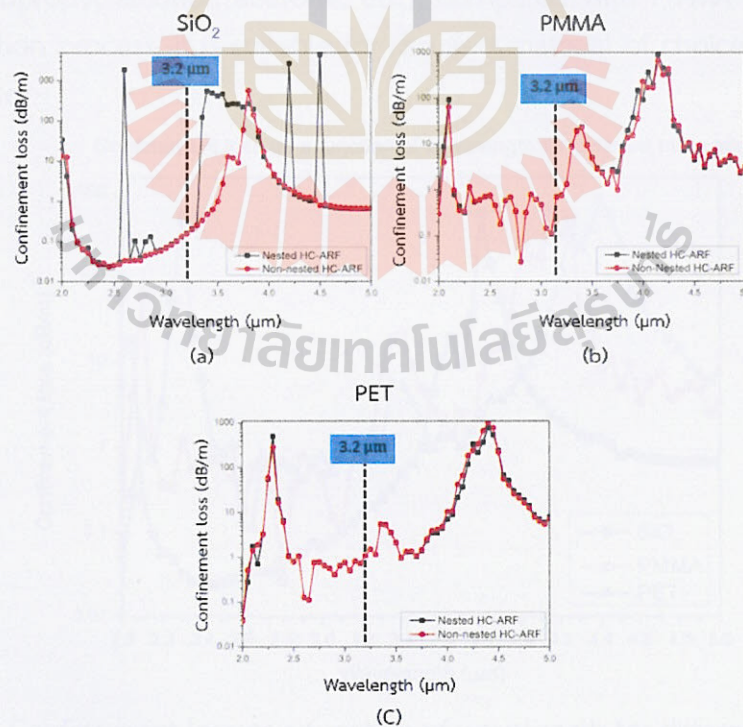

Figure 53 Confinement loss as function of wavelength for non-nested/nested HC-ARF with different material; (a) SiO₂, (b) PMMA, (c) PET.

4.2 Effect of changing cladding materials

SiO_2 is the fundamental material that is widely used to fabricate optical fiber while PMMA is a commercial polymer alike PET that is used for 3D printing techniques. So, after the non-nested structure is chosen, SiO2 and PMMA were used to compare the confinement loss and antiresonant window with PET material where they can be using an alternative material in the future.

The result in figure 54 showing that at the operating wavelength of 3.2 µm, the confinement loss is around 0.16, 0.75, and 1.06 dB/m for SiO2, PMMA, and PET, respectively. Considering the antiresonant window and the resonant peak, SiO_2 is smoother than PMMA and PET because in this band the imaginary part of the refractive index that affects the material absorption of SiO_2 is low and stable, while PMMA and PET are very high and fluctuate (see imaginary part of the refractive index of the material in appendix). PMMA fluctuates more than PET.

Although SiO2 presents a smoother and lower confinement loss, the PET material was chosen due to the aim of using the 3D printing technique for fiber fabrication in the future. For sensing purposes, PET was chosen as a material for optical fiber design and fabrication. Due to its chemical compatibility, which is non-dissoluble in basic chemicals (isopropyl alcohol, acetone, etc.), compared with PMMA for the surface functionalization process, it is suitable for use as a material of choice for the optical fiber gas sensor.
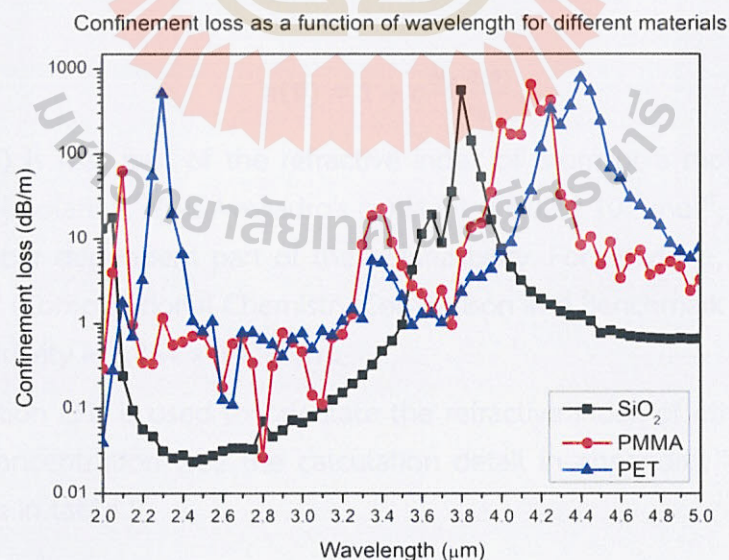

Figure 54 Confinement loss as a function of wavelength for different materials.

4.3 Ethylene gas sensing simulation results

The optimized structure of HC-ARF in this project is the non-nested structure, where the tube thickness is 2 µm, the diameter of the tube is 92 µm, the fiber air core diameter is 128 µm, and the overall fiber diameter is 340 µm. Confinement loss is around 1.06 dB/m for PET material. The optimized structure is shown in figure 55.
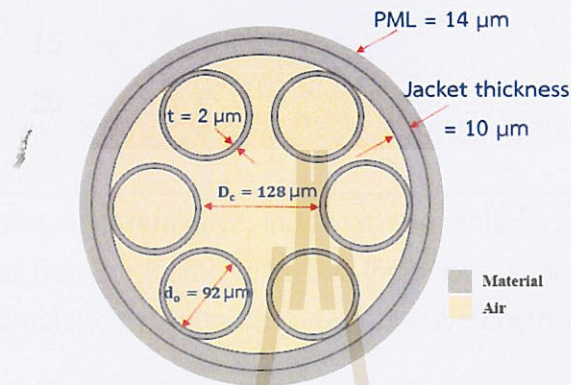

Figure 55 Optimized Structure of HC-ARF for guiding the wavelength of 3.2 µm.

To simulate the use of HC-ARF as the ethylene gas sensor, the refractive index inside the hollow core and cladding tube in figure 55 has changed to correspond with the ethylene concentration.

Using the relationship between electric susceptibility and polarizability and assuming there are no local field effects, we got the following equation: (Mayerhöfer, 2020)

$$n(\tilde{v}) = 1 + c\frac{N_A \cdot \acute{\alpha}(\tilde{v})}{2\varepsilon_0} . \tag{31}$$

when $n(\tilde{v})$ is real part of the refractive index of atom or a molecule, c is the concentration (molarity), N_A is Avogadro's constant $\approx 6.02 \times 10^{23}$ mol^{-1}, $\acute{\alpha}(\tilde{v})$ is the real and wavenumber dependent part of the polarizability. For ethylene, polarizability is equal 4.188 Å^3 (Computational Chemistry Comparison and Benchmark DataBase). ε_0 is vacuum permittivity $\approx 8.854 \times 10^{-12}$ F/m.

The equation (31) is used to calculate the refractive index of ethylene with the changing of concentration (see the calculation detail in appendix). The calculation result is shown in table 5.

Table 5 Relationship between concentration of ethylene gas and refractive index.

Ethylene (C_2H_4) concentration (ppm)	Refractive index
1	1.005
5	1.025
10	1.05
15	1.075
20	1.1
50	1.25

After calculation, the refractive index of the hollow core and cladding tube domains is changed from air to the refractive index of C_2H_4 in COMSOL (green area in figure 56(a). The simulation results after sweep wavelength 2-5 µm shown in figure 56(b).

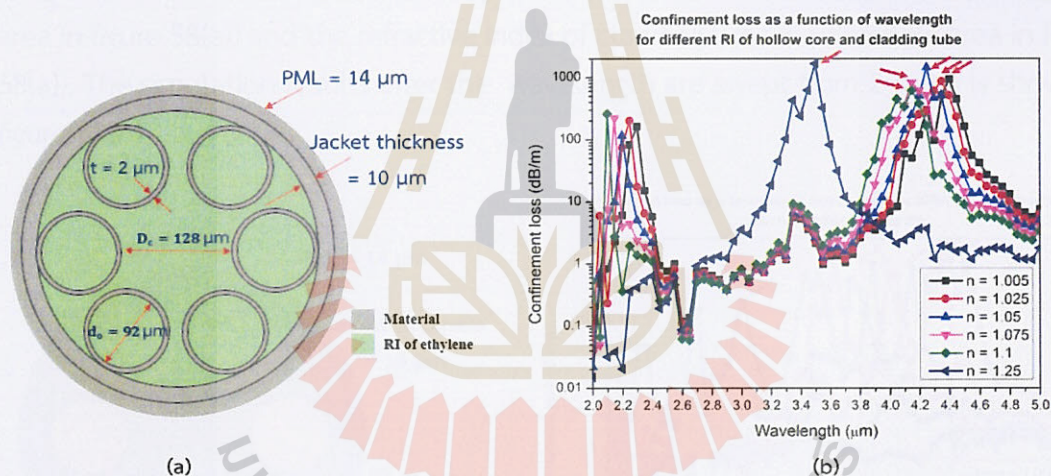(a)   (b)

Figure 56 a) The fiber structure with a changed refractive index of the green domain; b) Confinement loss as a function of wavelength with a changed refractive index of the green domain. (the red arrow indicates the resonance peak used in the sensitivity analysis.)

Results in figure 56(b) show that the resonance wavelengths are shifted to shorter wavelengths when the refractive index increase. To measure the sensitivity of the fiber, figure 57 shows the first resonant wavelength response with the refractive index of ethylene gas in each concentration. By using a linear fitting to find the slope of this graph, the result showing that the refractive index sensitivity is 3.66 µm/RIU when ethylene is filled in both hollow-core and the cladding tubes.
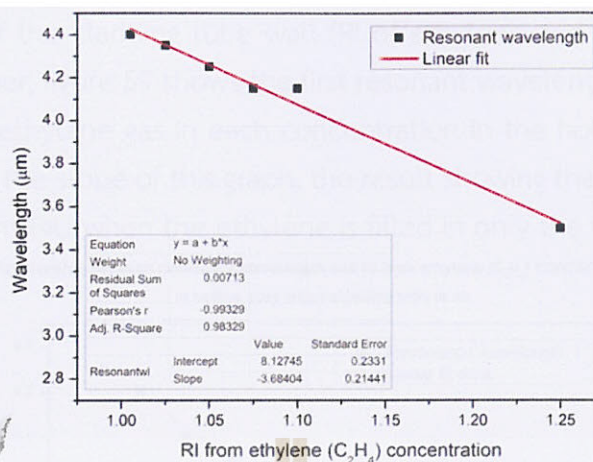
Figure 57 Relationship between first resonance wavelength and the RI value of ethylene concentration.

The sensitivity of HC-ARF when the ethylene is filled only in hollow-core was examined. The refractive index of ethylene is added in the hollow core domain (green area in figure 58(a)) and the refractive index of cladding tube is air (yellow area in figure 58(a)). The simulation results after the wavelength are swept from 2-5 μm is shown in figure 58(b).
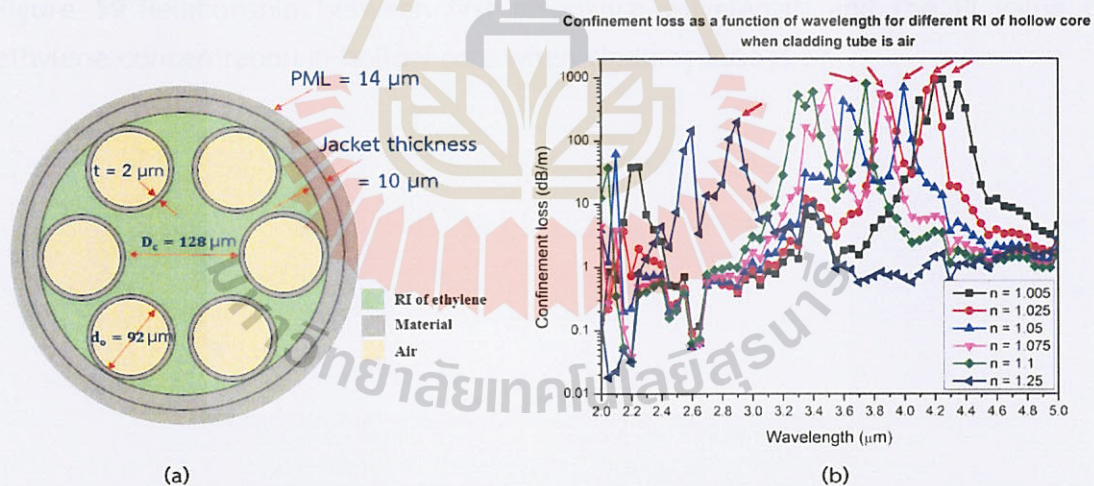

(a)   (b)

Figure 58 (a) The fiber structure with changed refractive indexes of ethylene showing as the green while the yellow domains is air; (b) Confinement loss as a function of wavelength with changed refractive indexes of the green domains. (The red arrow indicates the resonance peak used in the sensitivity analysis.)

The result in figure 58(b) shows that the resonance wavelengths are shifted to shorter wavelengths when the refractive index of the hollow increases. Compared with the graph in figure 56(b), the confinement loss of each refractive index revealed more number of resonant peaks and fluctuates. This causes by the different refractive index

of the two sides of the cladding tube wall (RI of ethylene and air). To measure the sensitivity of the fiber, figure 59 shows the first resonant wavelength response with the refractive index of ethylene gas in each concentration in the hollow core. By using a linear fitting to find the slope of this graph, the result showing that the refractive index sensitivity is 5.68 µm/RIU when the ethylene is filled in only the fiber core.
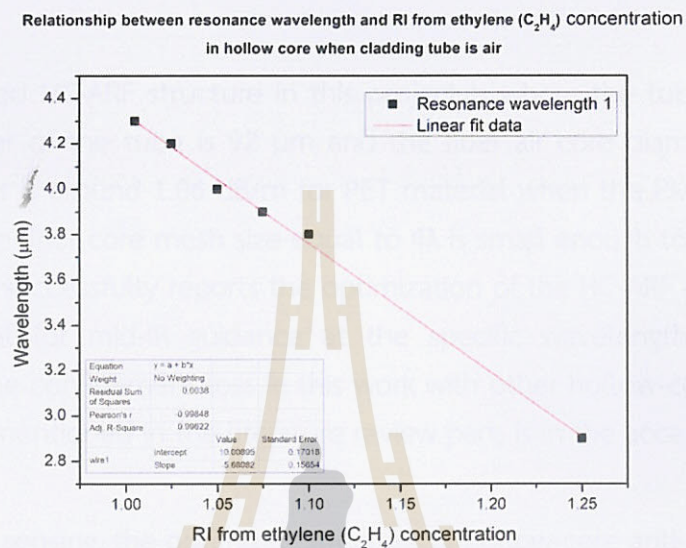

Figure 59 Relationship between first resonance wavelength and the RI value of ethylene concentration in hollow core when cladding tube is air.

CHAPTER V

CONCLUSION AND FUTRUE WORK

The optimized HC-ARF structure in this project is where the tube thickness is 2 μm, the diameter of the tube is 92 μm and the fiber air core diameter is 128 μm. Confinement loss is around 1.06 dB/m for PET material when the PML layer is equal to 14 μm and the fiber core mesh size equal to 4λ is small enough to get an accurate result. This work successfully reports the optimization of the HC-ARF design based on polymer material for mid-IR guidance at the specific wavelength of 3.2 μm. A comparison of the confinement loss in this work with other hollow-core fiber work in mid-IR, which is mentioned in the literature review part, is in the acceptable range (1– 5 dB/m).

For ethylene sensing, the optimized structure of hollow-core anti-resonant optical fiber can detect the change of concentration of ethylene gas (C_2H_4) when it was filled into the fiber by observing the shift of resonance wavelength. The peak resonant wavelengths are shifted to shorter wavelengths when the refractive index is increase which is corresponding with the increasing of concentration of ethylene gas. Overall refractive index sensitivity of the optimized fiber was reported. For the refractive index of the hollow core and cladding tube domains to be changed from air to the refractive index of C_2H_4, the overall sensitivity of 3.66 μm/RIU was achieved. For changing the refractive index of C_2H_4 in the hollow core domain while the refractive index cladding tube is fixed to be air, the overall sensitivity of the fiber sensor is 5.68 μm/RIU. This showing that, to fill the C_2H_4 inside the fiber core, the HC-ARF provides a higher ethylene sensitivity than filling in the C_2H_4 to both core and cladding tubes.

In future work, the optimized HC-ARF structure in this project will be fabricated and investigated with the light source at a wavelength of 3.2 μm. For the ethylene sensing investigation, we will flow the ethylene gas into the hollow core of the fiber because it has more sensitivity than flowing into both the hollow core and cladding tube.

REFERENCES

REFERENCES

Arismar Cerqueira, S. (2010). "Recent progress and novel applications of photonic crystal fibers." *Reports on Progress in Physics 73*(2), 024401.

Becker, M., Werner, M., Fitzau, O., Esser, D., Kobelke, J., Lorenz, A., Schwuchow, A., Rothhardt, M., Schuster, K., Hoffmann, D., and Bartelt, H. (2013). "Laser-drilled free-form silica fiber preforms for microstructured optical fibers." *Optical Fiber Technology 19,* 482-485.

Castrellon-Uribe, J. (2012). Optical Fiber Sensors: An Overview.

Chen, Y., Saleh, M., Joly, N., and Biancalana, F. (2016). "Guiding 2.94 µm using low-loss microstructured antiresonant triangular-core fibers." *Journal of Applied Physics 119,* 143104.

Cisco (2017). *Cisco Visual Networking Index: Forecast and Methodology 2016-2021. (2017)* Retrieved 25 January, 2023, from http://www.cisco.com/c/en/us/ solutions/collateral/ service-provider/visual-netwo rking-index-vni/complete-white-paper-c11-481360.html. High Efficiency Video Coding (HEVC) Algorithms and Architectures https:// jvet.hhi.fraunhofer.

Cristescu, S.M., Mandon, J., Arslanov, D., De Pessemier, J., Hermans, C., and Harren, F. (2013). "Current methods for detecting ethylene in plants." *Annals of botany 111*(3), 347-360.

Cruz, A., Serrão, V.A., Barbosa, C.L., Franco, M., Cordeiro, C., Argyros, A., and Tang, X. (2015). "3D printed hollow core fiber with negative curvature for terahertz applications". *Journal of Microwaves, Optoelectronics and Electromagnetic Applications.* 14. SI45-SI53

FOSCO. (2023). *"BASIC OPTICS FOR OPTICAL FIBER."* Retrieved 25 January, 2023, from https://www.fiberoptics4sale.com/blogs/archive-posts/95048070-basic-optics-for-optical-fiber.

Frei, W. (2015). *"Using Perfectly Matched Layers and Scattering Boundary Conditions for Wave Electromagnetics Problems."* From https://www.comsol. com/blogs/ using- perfectly-matched-layers-and-scattering-boundary-conditions-for-wave-electromagnetics-problems/.

Gattass, R.R., Rhonehouse, D., Gibson, D., McClain, C., Thapa, R., Nguyen, V.Q., Bayya, S., Weiblen, R., Menyuk, C., Shaw, L., and Sanghera, J. (2016). "Infrared glass-based negative-curvature anti-resonant fibers fabricated through extrusion." *Optics Express 24*(22), 25697-25703.

Hasanuzzaman, G.K.M., Christos, S., Markos, C., and Habib, M.S. (2018). "Hollow-core fiber with nested anti-resonant tubes for low-loss THz guidance." *Optics Communications 426*, 477-482.

Hossain, M.B., Bulbul, A., Mukit, M., and Podder, E. (2017). "Analysis of Optical Properties for Square, Circular and Hexagonal Photonic Crystal Fiber." *Optics and Photonics Journal 07*, 235-243.

Inc., F. (2021). *"Optical Fiber."* Retrieved 25 January, 2023, from https://www.f iberlabs .com/glossary/optical-fiber/.

Indian Institute of Technology, B. (2021). Fiber optics. Analysis of Wave-Model of Light, Prof. R.K. Shevgaonkar.

Ismail, M. (2009). Thermal Effects in Optical Fibers.

Izadpanah Toos, S. (2012). Fabrication of Optical fibers.

Jaworski, P., Koziol, P., Krzempek, K., Wu, D., Yu, F., Bojęś, P., Dudzik, G., Liao, M., Abramski, K., and Knight, J. (2020). "Antiresonant Hollow-Core Fiber-Based Dual Gas Sensor for Detection of Methane and Carbon Dioxide in the Near- and Mid-Infrared Regions." *Sensors 20*(14).

Joe, H.E., Yun, H., Jo, S. H., Jun, M., and Min, B.K.. (2018). "A review on optical fiber sensors for environmental monitoring." *International Journal of Precision Engineering and Manufacturing-Green Technology 5*, 173-191.

Kathirvelan, J. and Vijayaraghavan R. (2020). "Review on sensitive and selective ethylene detection methods for fruit ripening application." *Sensor Review ahead-of-print*.

Komanec, M., Dousek, D., Suslov, D., and Zvanovec, S. (2020). "Hollow-Core Optical Fibers." *Radioengineering 29*, 417-430.

Lu, J., Chen, Z., Pang, F., and Wang, T. (2008). "Theoretical Analysis of Fiber-Optic Evanescent Wave Sensors". 2008 *China-Japan Joint Microwave Conference*.

Mahad, F., Supa'at, A., Forsyth, D., Sun, T., and Azmi, A. (2016). "Characterization of erbium doped photonic crystal fiber." *TELKOMNIKA (Telecommunication Computing Electronics and Control) 14*, 880-886.

Mayerhöfer, T., Dabrowska, A., Schwaighofer, A., Lendl, B., and Popp, J. (2020). "Beyond Beer's law why the index of refraction depends (almost) linearly on concentration." *ChemPhysChem 21*, 10.1002/cphc.202000018.

Nadella, H.P., Joseph, E.S., and James, L.W. (1978). "Drawing and annealing of polypropylene fibers: Structural changes and mechanical properties." *Journal of Applied Polymer Science 22*(11), 3121-3133.

Okamoto, K. (2006a) Fundamentals of Optical Waveguides, *Elsevier Science.*

Okamoto, K. (2006b). Fundamentals of Optical Waveguides.

Pinto, A.M.R. and M. Lopez-Amo (2012). "Photonic Crystal Fibers for Sensing Applications." *Journal of Sensors 2012*, 598178.

Podder, E., Jibon, R., Hossain, M.B., Bulbul, A., Biswas, S., and Kabir, M. (2018). "Alcohol Sensing through Photonic Crystal Fiber at Different Temperature." *Optics and Photonics Journal 08*, 309-316.

Poletti, F. (2014). "Nested antiresonant nodeless hollow core fiber." *Optics Express 22(20)*, 23807-23828.

Putten, L.D.V. (2019). Design and Fabrication of Novel Polymer Antiresonant Waveguides, UNIVERSITY OF SOUTHAMPTON. Doctor of Philosophy, Ph.D.

RefractiveIndex. INFO (2008-2023). "Refractive index database." From https://refractive index .info/.

Richter, A., Paschew, G., Klatt, S., Lienig, J., Arndt, K.F., and Adler, H.J.P. (2008). "Review on Hydrogel-based pH Sensors and Microsensors." *Sensors 8*(1).

Rosenberger (2023). *"Singlemode or multimode glass fiber?".* Retrieved 25 January, 2023, from https://osi.rosenberger.com/news-media/singlemode-multimode-glass-fiber/.

Shahzadi, R., Shahzad, A., Qamar, F., Shahzadi, R., and Ali, M. (2018). *Effective Refractive Index and V-Parameter Characterization for Guided Modes in Multimode , Nano and Three Layer Optical Fibers.*

Silva, S., Roriz, P., and Frazão, O. (2014). "Refractive Index Measurement of Liquids Based on Microstructured Optical Fibers." *Photonics 1.*

Klorz, A., Janssen, S., and Lang, W. (2012). "Detection limit improvement for NDIR ethylene gas detectors using passive approaches." *Sensors and Actuators B: Chemical 175*, 246–254.

Talataisong, W. (2015). FABRICATION OF FIBER OPTIC TUNABLE FILTER BASED ON LONG PERIOD FIBER GRATING

Talataisong, W., Ismaeel, R., Beresna, M., and Brambilla, G. (2018). "Direct extrusion of suspended-core polymer optical fibers from 3D printers". *Frontiers in Optics / Laser Science, Washington, DC, Optical Society of America.*

Talataisong, W., Ismaeel, R., Sandoghchi, SR., Rutirawut, T., Topley, G, Beresna, M., and Brambilla, G. (2018). "Novel method for manufacturing optical fiber: extrusion and drawing of microstructured polymer optical fibers from a 3D printer." *Optics Express 26(24)*, 32007-32013.

Terai, T., Kubota, H., Miyoshi, Y., and Ohashi, M. (2019). "Core Diameter Dependence of Loss Characteristics in Anti-Resonant Hollow Core Fibers." *Asia Communications and Photonics Conference (ACPC) 2019, Chengdu, Optica Publishing Group.*

Wang, Y., Gao, R., and Xin X. (2021). "Hollow-core fiber refractive index sensor with high sensitivity and large dynamic range based on a multiple mode transmission mechanism." *Optics Express 29(13)*, 19703-19714.

Wikipedia (2023a). *"Bragg's law."* Retrieved 24 January, 2023, from https://en.wikipedia .org/wiki/Bragg%27s_law.

Wikipedia (2023b). *"Core (optical fiber)."* From https://en.wikipedia.org/wiki/Core_(optical_fiber).

Wikipedia (2023c). *"Fabry–Pérot interferometer."* 2022, from https://en.wikipedia .org/wiki/Fabry%E2%80%93P%C3%A9rot_interferometer.

Yakasai, I.K., Rahman, A.U., Abas, P.E., and Begum, F. (2018). "Theoretical Assessment of a Porous Core Photonic Crystal Fiber for Terahertz Wave Propagation." *Journal of Optical Communications 43.*

Yang, X., Lu, Y., Liu, B., and Yao, J. (2017). "Analysis of Graphene-Based Photonic Crystal Fiber Sensor Using Birefringence and Surface Plasmon Resonance". *Plasmonics, 12*, 489-496.

Yu, R., Chen, Y., Shui, L., and Xiao, L. (2020). "Hollow-Core Photonic Crystal Fiber Gas Sensing." *Sensors 20*(10).

APPENDICES
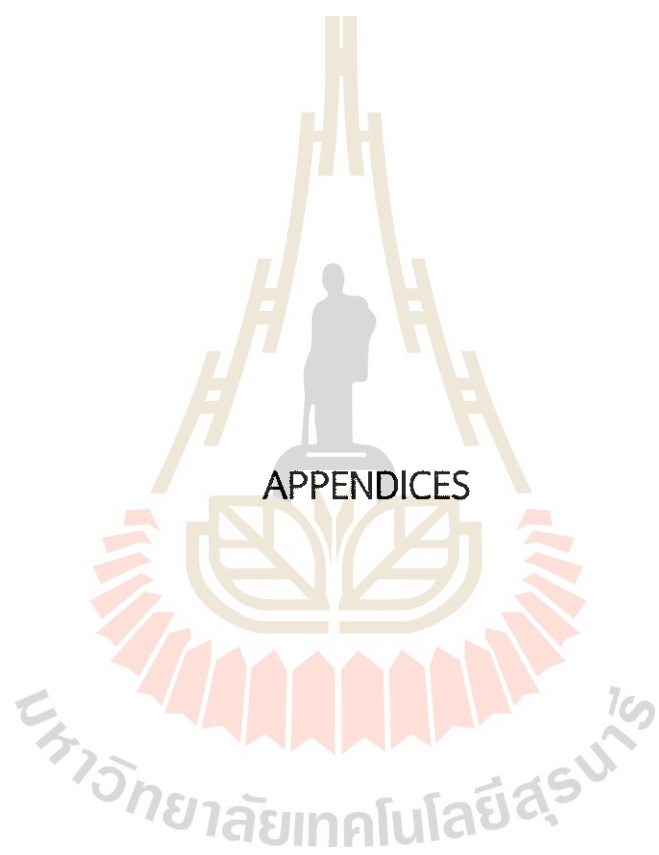
APPENDIX A
CONVENTIONAL OPTICAL FIBER

Optical fiber is known as a useful device for data transfer in telecommunication, which has been invented and developed for more than 50 years. To date, the optical fiber more applications of optical fiber have been developed especially for sensing applications due to its light weight, small size, no electrical power is needed at the remote location, and can be multiplexed used with many sensors along the length of a fiber by using light wavelength shift for each sensor. Many techniques have been developed to fabricate the optical fiber sensor such as the fabrication of fiber Bragg grating, the fabrication of micro/nano optical fiber taper, the fabrication of optical fiber resonator and the microstructured optical fiber.

An overview of the conventional optical fiber including the fundamental structure, guiding principle, and fabrication process will be presented in the following section.

Structure of conventional optical fiber

Optical fiber is an optical device used for the light guiding inside the optical fiber. Typical structure of the conventional optical fiber consists of core and cladding as shown in figure A-1, where the refractive index of core material is slightly greater than the cladding ($\sim 10^{-3}$). In general, the core and the cladding layers are usually made of silica or plastic. Figure A-1 shows the schematic cross-section of conventional optical fiber for telecommunication used. The layers 1 and 2 in figure A-1 are the core and cladding, respectively while the outer 2 layers are the buffer and the jacket which are used for the fiber protection propose.
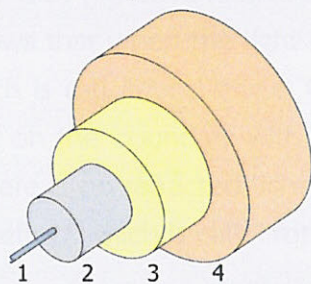
Conventional optical fibers component consists of (1) Core, (2) Cladding, (3) Buffer, and (4) Jacket

Figure A-1 Optical fiber components. (Wikipedia, 2023a)

Guiding principle in the conventional optical fiber

Light can be propagated through the optical fiber based on the total internal reflection (TIR) at the boundary between the core and cladding. To be consistent with the TIR, the refractive index of the core (n_1) must greater than the refractive index of the cladding (n_2). Following this principle, the incident angle of light at the boundary between the core and cladding must larger than the critical angle to achieve the TIR of reflected light, which is defined by the refractive indices of the guided mediums and surrounding medium based on Snell's Laws.
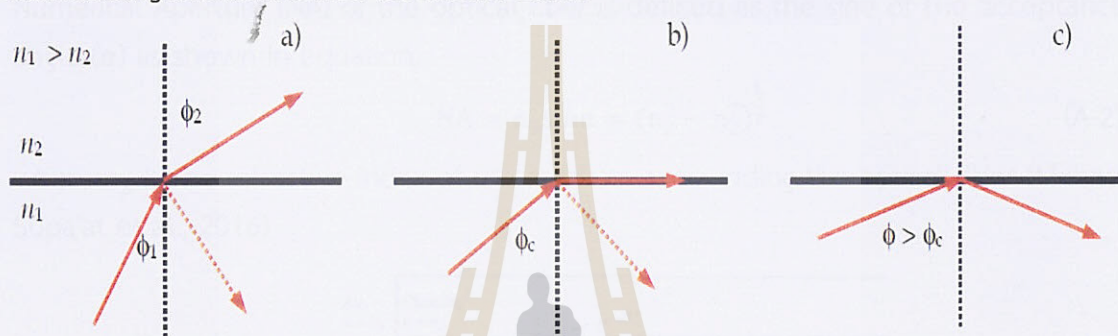
Figure A-2 Light travelling from medium 1 (n_1) to medium 2 (n_2) when $n_1 > n_2$ (a) The incident angle ($\emptyset_1$) is lower than the critical angle ($\emptyset_c$ showing the reflection and refraction of light at boundary. (b) The incident angle ($\emptyset_1$ is equal to the critical angle ($\emptyset_c$) where the refracted angle $\emptyset_2 = 90°$. (c) The total internal reflection occurred when $\emptyset_1 > \emptyset_c$.

The diagram in figure A-2(a) showing that light incident at the boundary between 2 mediums with different refractive indices can be reflected and refracted at the boundary. Reflection angle will be the same as incident angle ($\emptyset_1$) while the angle of refraction ($\emptyset_2$) can be defined by the Snell's law as presented below.

$$n_1 \sin \emptyset_1 = n_2 \sin \emptyset_2. \tag{A-1}$$

Based on the Snell's law, the angle of refraction of the light travelling from the medium with higher refractive index will be larger than the incident angle. Figure A-2(b) shows that when the light is incident at the boundary with the incident angle of $\emptyset_c$, which is call critical angle, the angle of refraction is $\emptyset_2 = 90°$. When the light is incident on the boundary with the incident angle is larger than the critical angle ($\emptyset_1 > \emptyset_c$), there is no refracted light in the second medium. Hence, the incident light will totally reflect which is call "Total internal reflection".

Considering the propagation of light in the conventional optical fiber, $\emptyset_c$ of light at the core-cladding boundary is related to the acceptance angle (α) of the optical fiber. Acceptance angle is the maximum incident angle of light at the fiber facet where the light is satisfied the total internal reflection at core-cladding boundary as shown in figure A-3. It can be calculated by using the refractive index of the fiber core, cladding and the environment surround the optical fiber. Light incident at the fiber facet with an angle larger than α will not meet the requirement to propagate through the optical fiber because the incident angle between core and cladding is smaller than $\emptyset_c$. The Numerical Aperture (NA) of the optical fiber is defined as the sine of the acceptance angle (α) as shown in equation,

$$NA = n_3 \sin\alpha = (n_1^2 - n_2^2)^{\frac{1}{2}} . \tag{A-2}$$

where n_3 is the refractive index of the medium surrounding the optical fiber (Mahad, Supa'at et al., 2016)
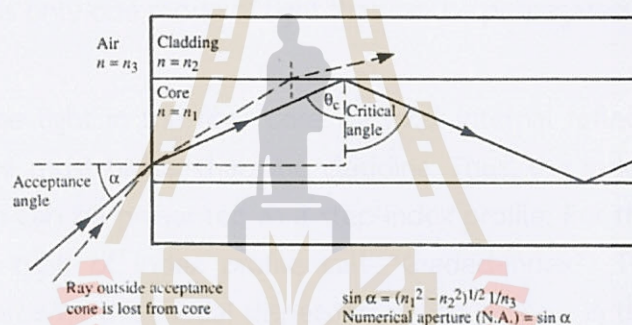
Figure A-3 Optical Fiber's Acceptance Angle and Numerical Aperture. (FOSCO, 2023)

Type of optical fiber classified by the guided mode.

Light wave is an electromagnetic (EM) wave, which can be described by Maxwell's equation. The EM wave composed of electric and magnetic fields, which are perpendicular to each other and to the direction of propagation. Conventional optical fiber can be classified into two main types based on the number of guided modes in the fiber core: a single-mode fiber and a multimode fiber. The single-mode fiber is the optical fiber designed for only one guided mode of light to be propagated along the fiber core, on the other hand, the multimode fiber is the optical fiber designed to allow the propagation of more than one mode of light.
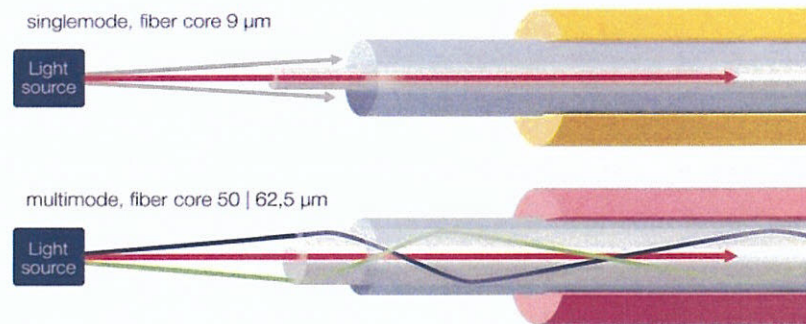
Figure A-4 Mode of fiber, sigle mode (above) and multimode (below). (Rosenberger, 2023)

Figure A-4 shows the comparison of light propagating in the fiber between single-mode and multimode fibers. As shown in the figure A-4(a), the single-mode fiber has a smaller core size comparing with a multimode fiber to only allow the light to propagate along the central part of fiber, and there are no longer different velocities for different modes. So, there is only one mode of light that can be propagated through the optical fiber.

To confine the light in the fiber core via total internal reflection, the refractive index of fiber core must higher than the cladding. Thus, the index profile along the fiber cross-section can be presented as a step-index profile. For the multimode fiber, there is another type of index profile call "Graded-index". This fiber has been developed to overcome the modal dispersion, which is occur in the multimode step-index fiber. Therefore, by classifying the optical fiber based on the index profile, the optical fiber can be separated to the step-index fiber and graded-index fiber as presented in figure A-5.
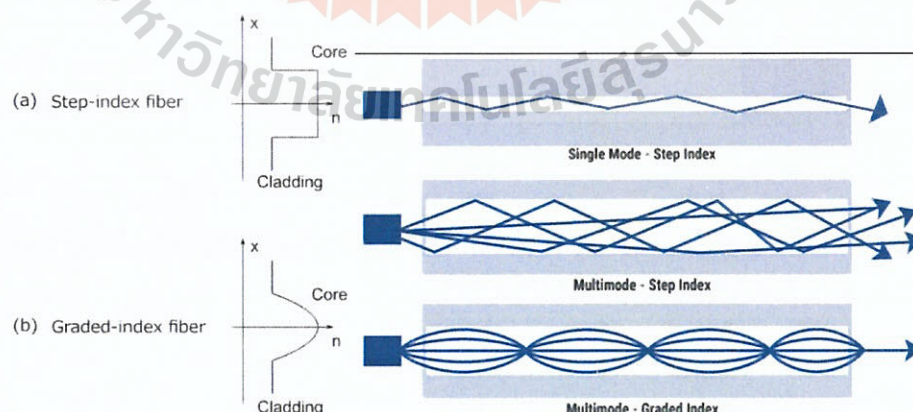
Figure A-5 Type of optical fiber when classifying by the index-profile including (a) step-index and (b) the graded-index fiber. (Inc, 2021)

Figure A-5 shows two different index profiles of optical fiber, the step index, and the graded index fiber. The step-index fiber is the optical fiber that the refractive index of the fiber core is uniformly and instantly changes at the boundary between core and cladding region. The graded-index fiber is the optical fiber that has a maximum refractive index at the center of the core. The core refractive index of the graded-index fiber is not uniform but will be gradually decreased from the center to cladding. In step-index fiber, the multi-mode has signal dispersion at the end of the fiber but not in the single-mode. The gradually change in the refractive index of graded-index fiber can improve the dispersion of the multi-signal.

Allowed modes of light that can be propagated along the waveguide are described by considering the light as the electromagnetic waves. In the waveguide, allowed modes of light consist of a transverse electromagnetic (TEM) mode, a transverse electric (TE) mode, a transverse magnetic (TM) mode, and a hybrid mode. The TEM mode is the mode where neither electric nor magnetic field are in the direction of propagation, The TE and TM modes are the modes when there is no electric field and no magnetic field in the direction of propagation, respectively. The hybrid mode is the modes when both electric and magnetic fields are in the direction of propagation.

The analyzation of TE, TM, TEM, and hybrid modes in the step-index optical fiber can be describes by the Maxwell's equations when the refractive index of core is higher than the cladding. For conventional optical fiber, the refractive index different between core (n_1) and cladding (n_2) is of the order of ~ 0.3-0.8%. So, the index ration between core and cladding can be approximated to be $n_1/n_2 \cong 1$. This approximation was designated to simplify the analysis of optical fibers drastically. The analysis of allowed modes in optical fiber based on this approximation were designated as linearly polarized (LP$_{lm}$) mode where l and m are azimuthal and radial indices, respectively. This approximation is called the weakly guiding approximation because, light confinement in the core is not so tight. Therefore, light energy would be almost uniformly distributed in the entire core and exponentially decreased when entering the cladding region.

In the optical fiber, light travels in the form of transverse electromagnetic waves. Thus, the longitudinal components of the fields vanish. However, this disappearance cannot occur immediately. So, when the value of n_1 approaches the value of n_2, the longitudinal components of the fields get weaker, and finally, the waves get

transformed into transverse electromagnetic waves. Therefore, for a practical fiber, where the refractive index difference is very small (Δn~ 0.3-0.8%.), the longitudinal components are also negligibly small. Thus, the longitudinal electric and magnetic fields approach 0 ($E_z, H_z \rightarrow 0$). For most of the practical fibers, the weakly guiding approximation is well applicable and justified because the difference between the core and cladding refractive indices is very small. In other words, the fields in a practical optical fiber are almost transverse in nature and it can be shown that they are linearly polarized (Indian Institute of Technology, 2021) as shown In figure A-6.
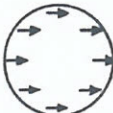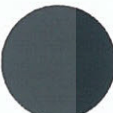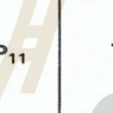
Figure A-6 Electric field vectors and intensity profiles of LP modes and conventional modes. (Okamoto, 2006a)

The dispersion equation under weakly guiding approximation is solved to analyze the mode propagation in the optical fiber (Okamoto, 2006b). The normalized frequency, or v number, is a parameter obtained from the dispersion equation, which can be defined by the optical fiber structure, including the properties of the core and the cladding and the wavelength of the light as presented below.

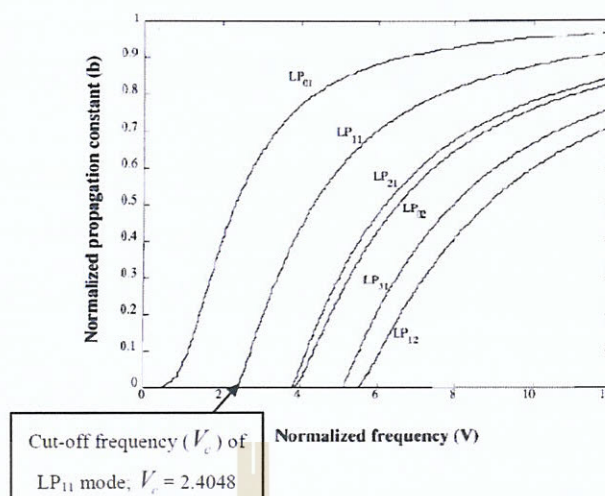$$v = \frac{2\pi a}{\lambda} \sqrt{n_1^2 - n_2^2} \,. \tag{A-3}$$

Figure A-7 Graph between normalized propagation constant (b) and Normalized Frequency (V) of the linear polarized mode in optical fiber. (TALATAISONG, 2015)

Considering the graph in figure A-7, the cut-of frequency (v_c) of each mode is defined at the position where the value of normalized propagation constant (b) of each mode is occurred. As shows in the graph, the normalized propagation constant (b) of LP_{11} mode occur at the normalized frequency of 2.4048 (Shahzadi, shahzad et al., 2018), thus, at the normalized frequency lower that 2.4048, there is only LP_{01} mode guided in the optical fiber. Hence, the single-mode operation in the optical fiber is occurred when normalized frequency is lower than 2.4048 where only LP_{01} mode can propagate in the fiber core, and it is called as the fundamental mode.

Fabrication of Optical Fibers

In the traditional technique for optical fibre fabrication, two essential processes are required. The first process is the fabrication of fiber preform to form the optical fiber structure such as a cylindrical rod of silica with different refractive indexes between core and cladding or a cylindrical rod with the specific structure inside the preform. The second process is the fiber drawing process, which is used to shrink down the large fiber preform to the scale of the optical fiber.

Fiber preforms fabrication process.

Many techniques to fabricate the optical fiber preform have been developed for the fabrication of various types of the optical fiber including a vapor phase oxidation and a direct-melt technique.

- Vapor phase oxidation

Vapor phase oxidation is the traditional technique to fabricate the fiber preform. In the preform fabrication process, a large glass tube will be rotated while reactants will be flown through the tube and a burner, which will heat the tube from the side (figure A-8), applying the external heat. The Chemical vapors (oxidizable vapors) in the tube are converted to soot particles that adhere to the inside of the tube to form glassy layers, which will become a fiber core.
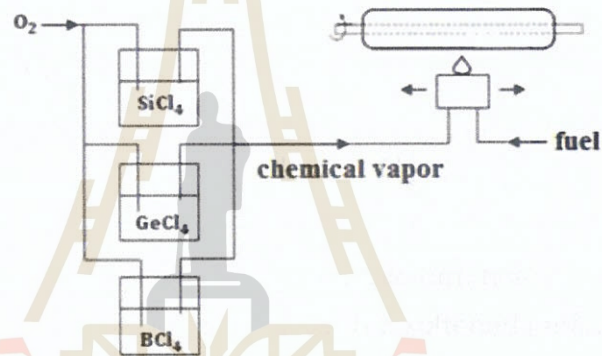

Figure A-8 Fiber preform fabrication with Vapor phase oxidation. (Izadpanah Toos, 2012)

- Direct-melt process

The direct process is a technique to fabricate the optical fiber preform from the melting glass rod. The material for fabricating the core and cladding will be added in separated crucibles as presented in figure A-9. The glass rods for core and cladding region will then be extruded from the melted silica which is heated by using the furnace. In the next process, the fiber can be drawn directly from the molten state.
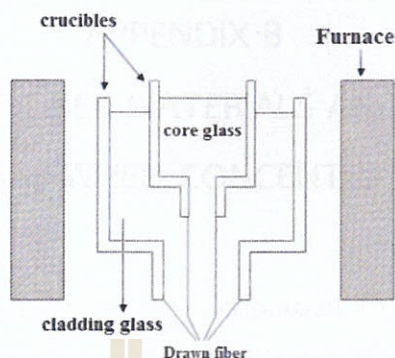
Figure A-9 Fiber preform fabrication with Double crucible method. (Izadpanah Toos, 2012)

Optical fiber drawing process

To minimize the optical fiber, preform to the optical fiber size, the fiber drawing process is required. Figure A-10 shows the standard process to draw the fiber preform to the desired fiber size. In the fiber drawing process, the preform glass rod, including core and cladding layer, will be connected to the preform holder. Then, the preform will be fed into the furnace to heat up the silica. The softened preform glass will then be pulled by using the tractor system. Diameter gauge is placed after the furnace to monitor the diameter of drawn fiber. The coating cone is used to coat the fiber with UV curable polymer. The polymer will be cured with a UV lamp to protect the bare fiber from contaminated environments, such as dust and water vapor. (Izadpanah Toos, 2012)
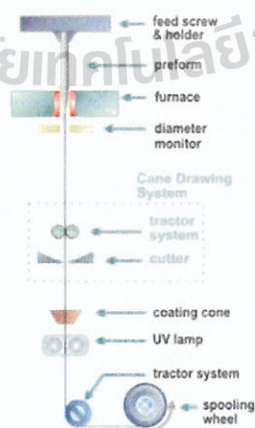

Figure A-10 Fiber drawing tower. (Izadpanah Toos, 2012)

APPENDIX B

REFRACTIVE INDEX OF FIBER MATERIALS AND REFRACTIVE INDEX

OF ETHYLENE GAS WHEN CONCENTRATION CHANGE

The refractive index of the material is important for material absorption loss, especially in the imaginary part. So, in this section, we will show and explain about a graph that presents the variation of the real and imaginary parts of the refractive index of PET, PMMA, and SiO_2 with the wavelength in the mid-IR region. In this section, we also examined the refractive index of ethylene gas that varies with its concentration. The calculation of the refractive index as a function of ethylene concentration is demonstrated.

Refractive index of fiber materials

The complex refractive index of SiO_2 is shown in figure B-1. The graph has extremely change around 7.5 μm. At around our operating wavelength of 3.2 μm, the real part of the refractive index is gradually changing. The imaginary part is not clear enough to detect the change. The value of the imaginary part around that wavelength is low, around 10^{-4}. So, that is the reason why we get the smoothest graph and the lowest loss as shown in figure B-4 compared with PMMA and PET at a wavelength range of 2–5 μm.
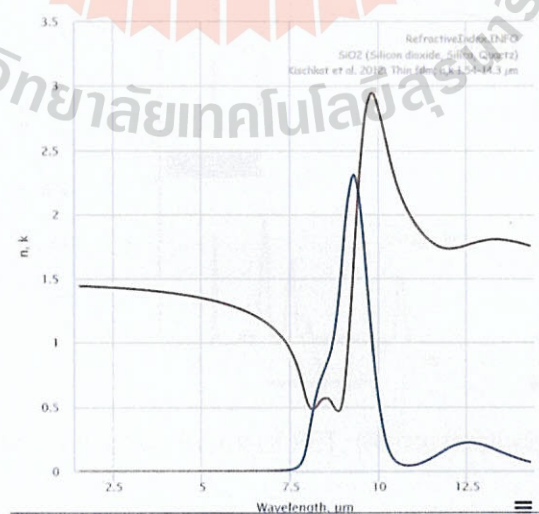

Figure B-1 Complex refractive index of SiO_2. (RefractiveIndex.INFO, 2008-2023)

For PMMA and PET, the complex refractive index very much fluctuates in the mid-IR regime, especially in the wavelength range of 6–15 μm. Around our operating wavelength of 3-3.5 μm, the refractive index does not fluctuate as much. However, we can see some peaks around that wavelength, as shown in figure B-2 and B-3. PMMA, which has a higher and wider peak in the imaginary part of the refractive index than PET, provides higher fluctuation and confinement loss, as shown in figure B-4.
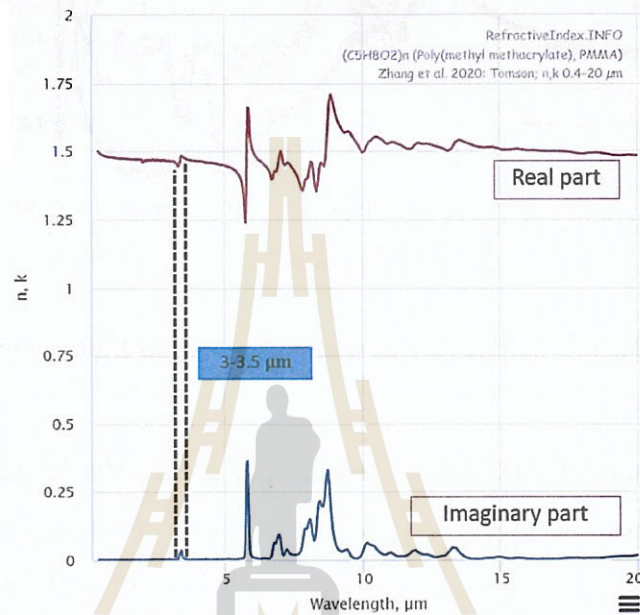

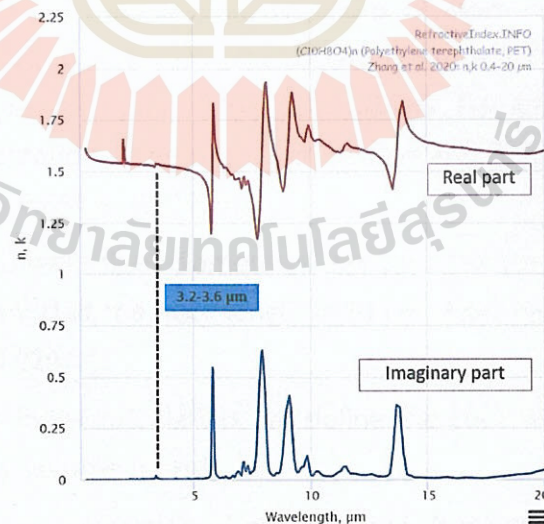**Figure B-2** Complex refractive index of PMMA. (RefractiveIndex.INFO, 2008-2023)

Figure B-3 Complex refractive index of PET. (RefractiveIndex.INFO, 2008-2023)
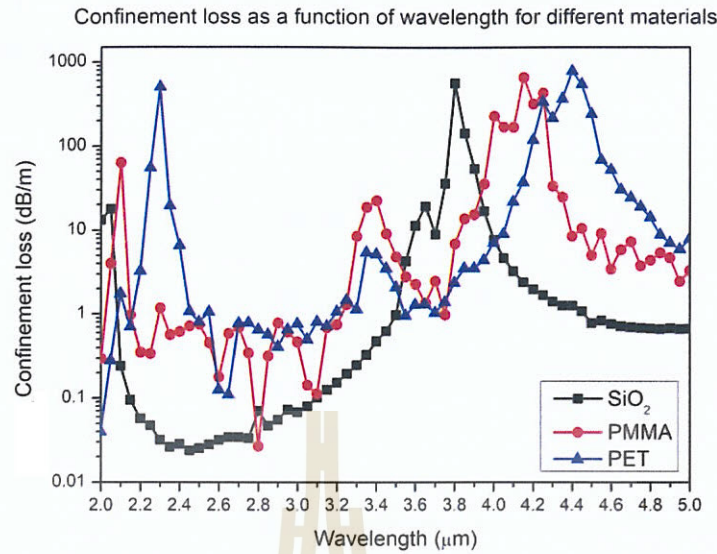
Confinement loss as a function of wavelength for different materials

Figure B-4 Confinement loss as a function of wavelength for different materials.

Refractive index of ethylene (C₂H₄) gas when concentration change

The equation below was used to calculate the real part of the refractive index of gas while concentrations were changing.

$$n(\tilde{v}) = 1 + c\frac{N_A \cdot \dot{\alpha}(\tilde{v})}{2\varepsilon_0}$$ (B-1)

When $n(\tilde{v})$ is real part of the refractive index of atom or a molecule, c is the concentration (molarity), N_A is Avogadro's constant $\approx 6.02 \times 10^{23}$ mol⁻¹, $\dot{\alpha}(\tilde{v})$ is the real and wavenumber dependent part of the polarizability. For ethylene, polarizability is equal 4.188 Å³ (Computational Chemistry Comparison and Benchmark DataBase). ε_0 is vacuum permittivity $\approx 8.854 \times 10^{-12}$ F/m.

In this work, the overall fiber diameter is 228 μm. The cladding tube diameter is 96 μm. And we assume that the fiber length is 10 cm. After calculation, our fiber has a volume of around 4.024 μL.

For the refractive index calculation, we define the concentration of gas in a unit of parts per million by volume (ppm).

For example, the concentration of gas is 1 ppm, it means that if the volume of fiber core is 10^6 μL, it has C₂H₄ equal to 1 μg. For our fiber that has a volume of around 4.024 μL, the amount of C₂H₄ equal to $\frac{1\,\mu g \times 4.024\,\mu L}{10^6\,\mu L} = 4.024 \times 10^{-6}$ μg

Then, change the amount of gas to Molarity, it equal to $\frac{4.024 \times 10^{-6}\,\mu g}{28 \times 4.024\,\mu L} = \frac{1}{28} \times 10^{-6}\ mol/L$.

Following the equation (B-1),

$$n(\tilde{v}) = 1 + \left[\left(\frac{1}{28} \times 10^{-6}\right)\left(\frac{6.02 \times 10^{-23} \times 4.18 \times 10^{-30}}{2(8.854 \times 10^{-12})}\right)\right] = 1.005$$

So, C_2H_4 1 ppm has the refractive index equal to 1.005

CURRICULUM VITAE

Name : Kwanjira Joonmasa

Date of Birth : 16 August 1996

Place of Birth : Fort Suranari Hospital, Nakhonratchasima

Education : Bachelor's degree in Physics (2015 – 2019), Suranaree University of Technology, Thailand Bachelor of Science (Physics), Honors Program (First class honors), GPA = 3.72/4.00

Master's degree in Applied Physics (2019 – Present) Suranaree University of Technology, GPA = 3.77/4.00

Publications : Siam Physics Congress 2022: Carbon Neutrality (SPC 2022)

Awards : -

Grants and Fellowships : Scholarship supported by Suranaree University of Technology until 2021.

Position and Place of Work : -